nature portfolio

https://doi.org/10.1038/s41565-021-00947-8

Supplementary information

Progressive growth of the solid–electrolyte interphase towards the Si anode interior causes capacity fading

In the format provided by the authors and unedited

Supplementary Information for

Solid-electrolyte interphase progressive growth towards the Si interior to cause capacity fading

Yang et al.

The Supplementary Information includes:

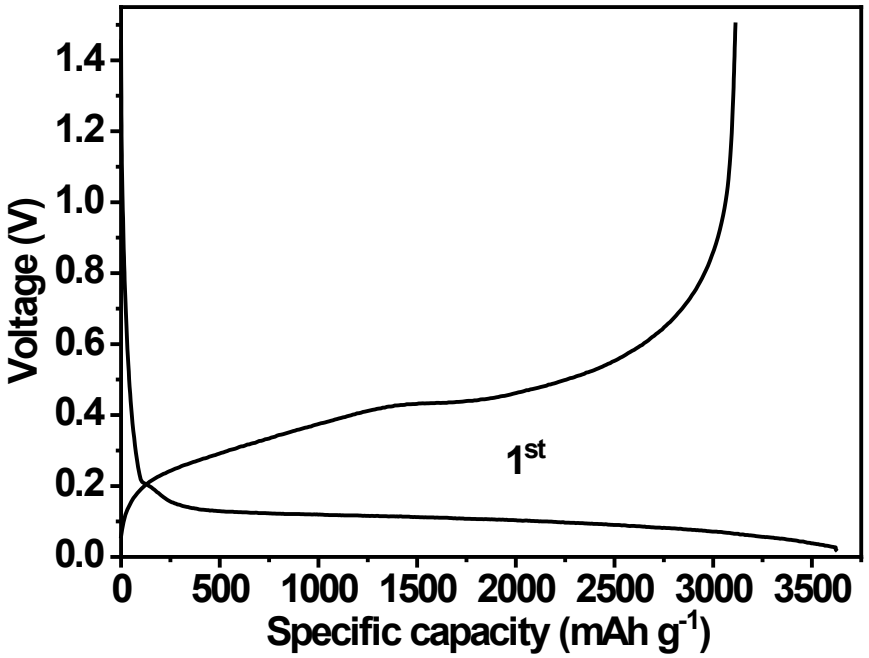

Supplementary Fig. 1 | Voltage profiles for the first galvanostatic cycles of the Si nanowires.

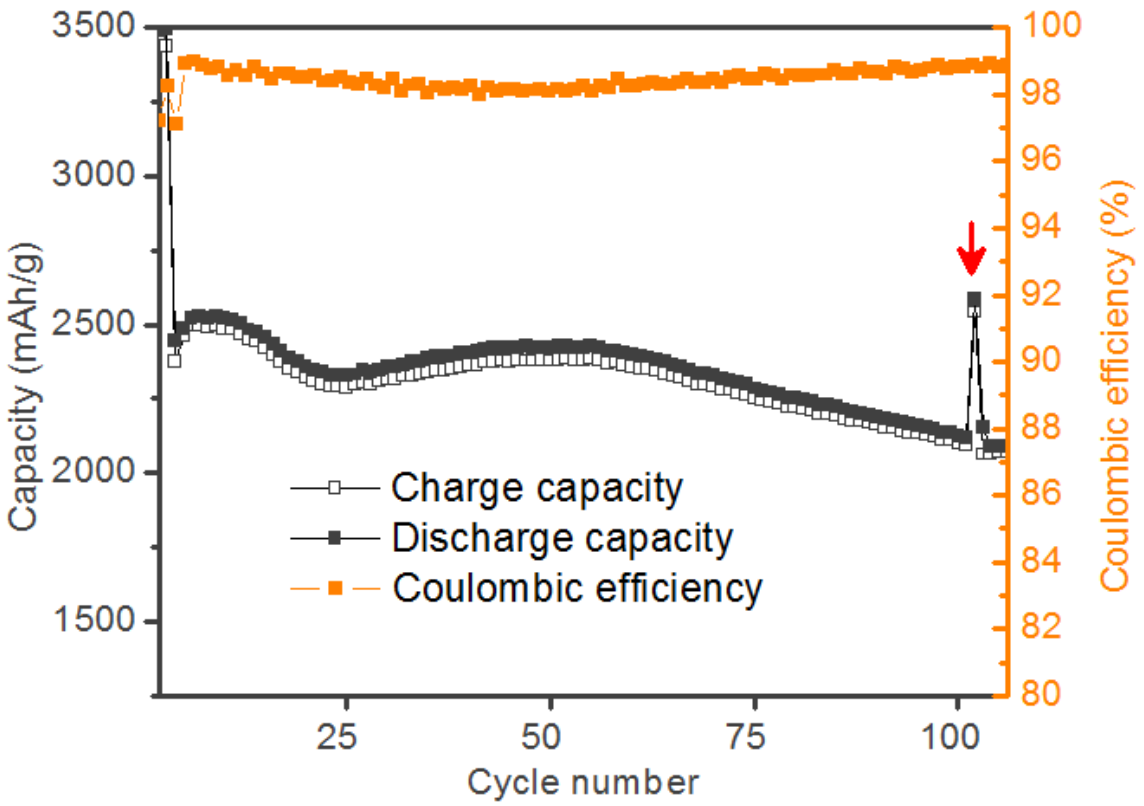

Supplementary Fig. 2 | Capacity and Coulombic efficiency evolution curves of another cell. We used 0.02C charge/discharge rate in the first two cycles and then cycled the nanowire at 1C for 98 cycles and then checked the capacity of the cell on the 101th cycle by using a much lower 0.02C discharge rate (as indicated by the red arrow). Clearly, the capacity loss from the increased impedance within the core is partly redeemed. Note that the capacity is averaged over total weight of the Si nanowires on the electrode.

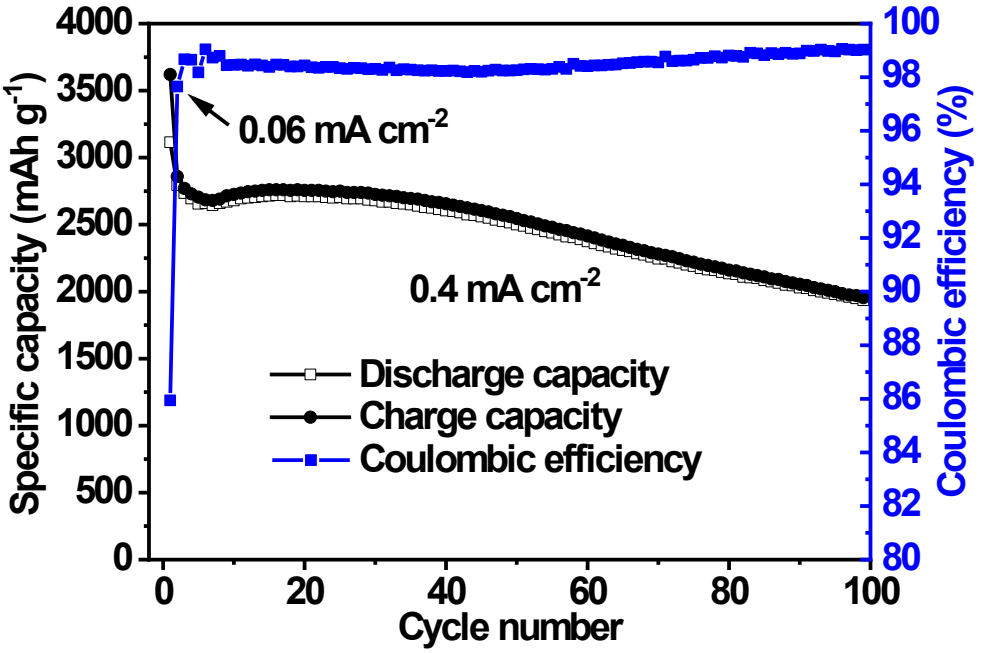

Supplementary Fig. 3 | Capacity and Coulombic efficiency as a function of cycle numbers for the Si nanowires.

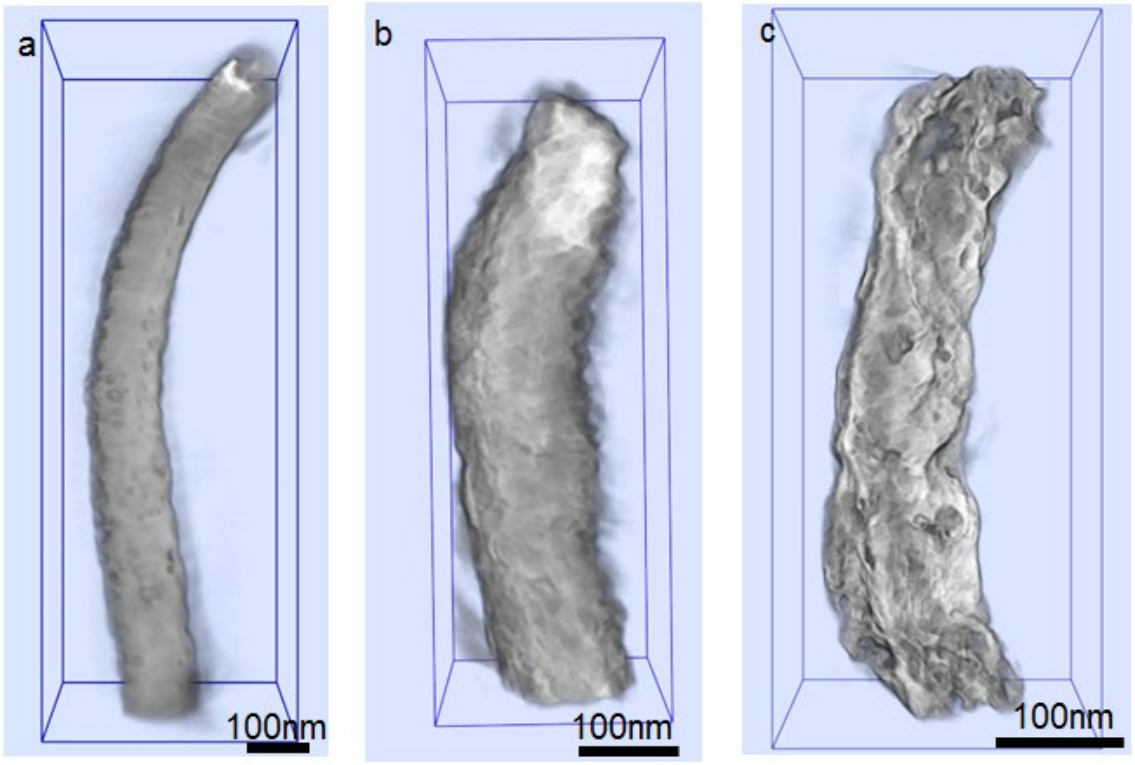

Supplementary Fig. 4 | Cryo-STEM HAADF tomography Si nanowires after 1st (a), 36th (b) and 100th cycles (c). Clearly, openings from surface to the interior of the nanowire gradually appeared after extensive cycling which can facilitate the permeation of the electrolyte molecules and hence inward growth of the SEI.

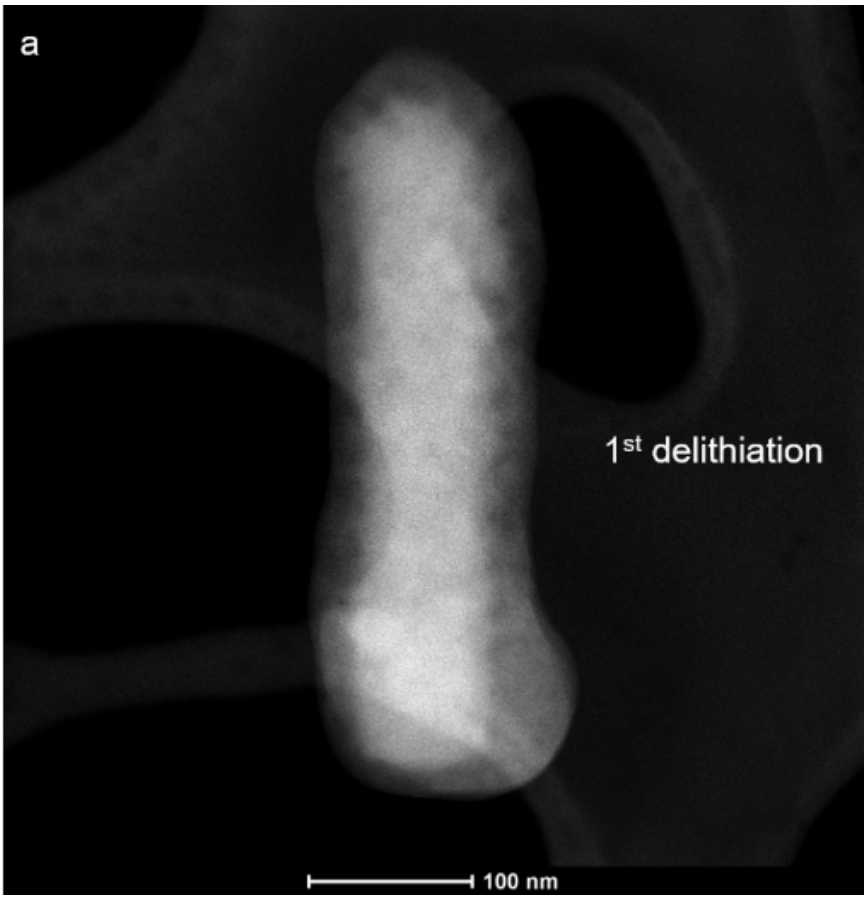
a
1st delithiation
100 nm

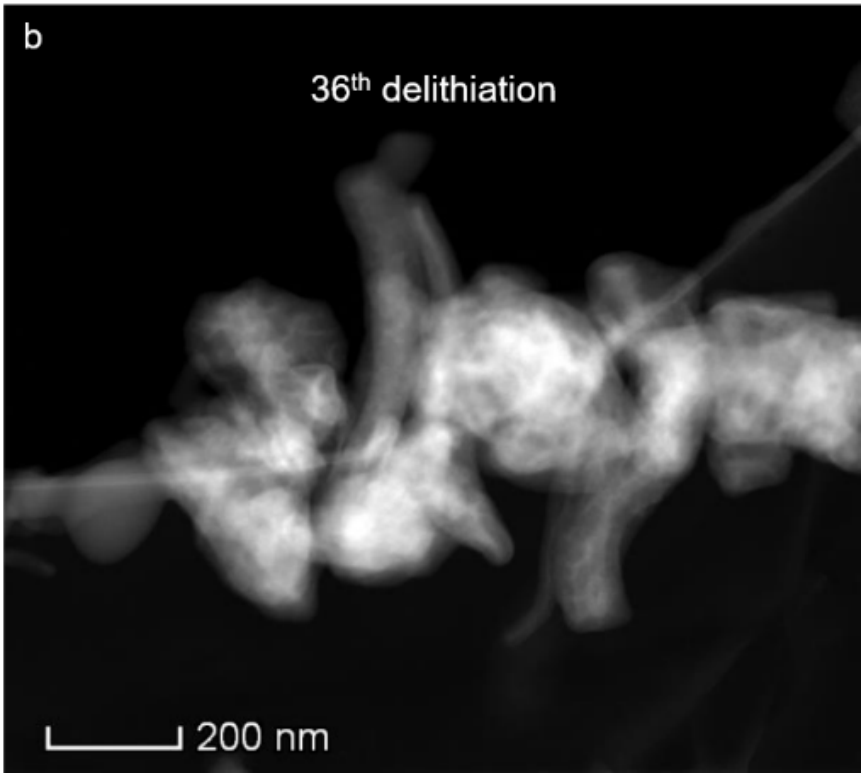
b
36th delithiation
200 nm

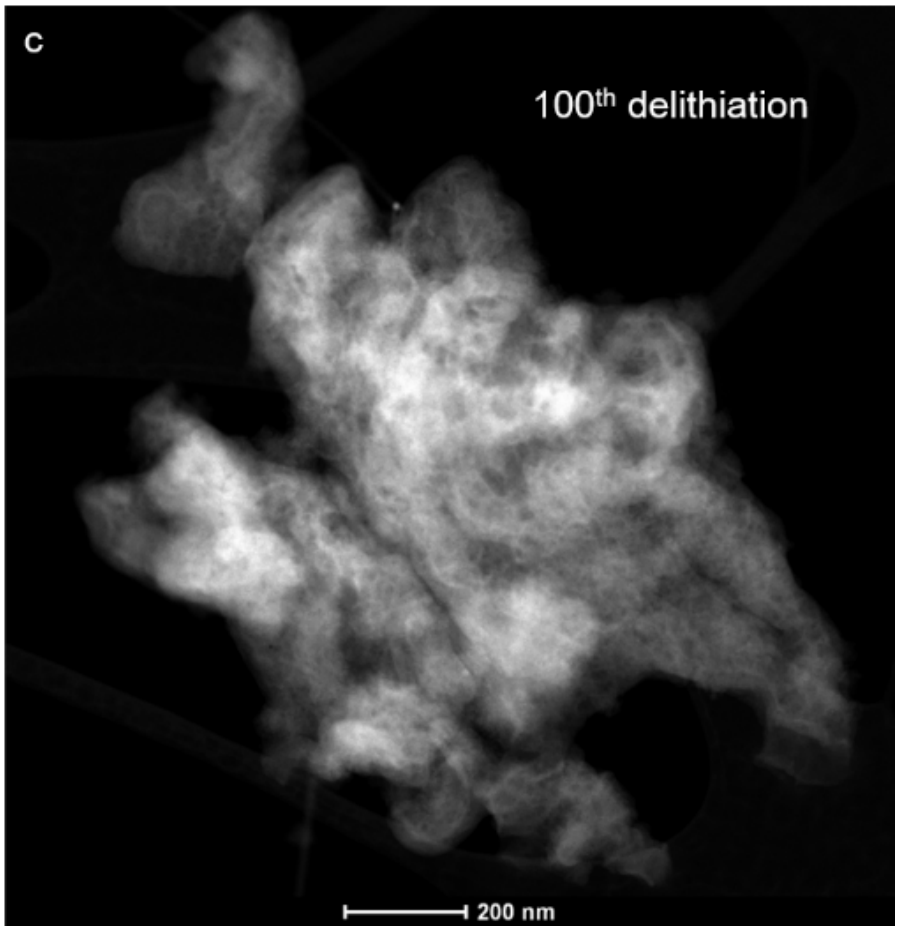

Supplementary Fig. 5 | Additional STEM-HAADF images of delithiated Si nanowires after different cycles to reveal the general feature of Si upon cycling. (a) 1st delithiated, (b) 36th delithiated, and (c) 100th delithiated. It should be pointed out that, the nanowires are not uniform in diameter and with long term cycling, the nanowire deform due to the growth of SEI towards the interior of Si. Also, for the Cryo-TEM sample preparation, we scratch off the sample. All these factors compounding together to make the sample loss the nanowire morphology, which is especially true for the sample following the extended cycling, as evidenced by comparing the case from 1 cycle, to 36 cycles and 100 cycles.

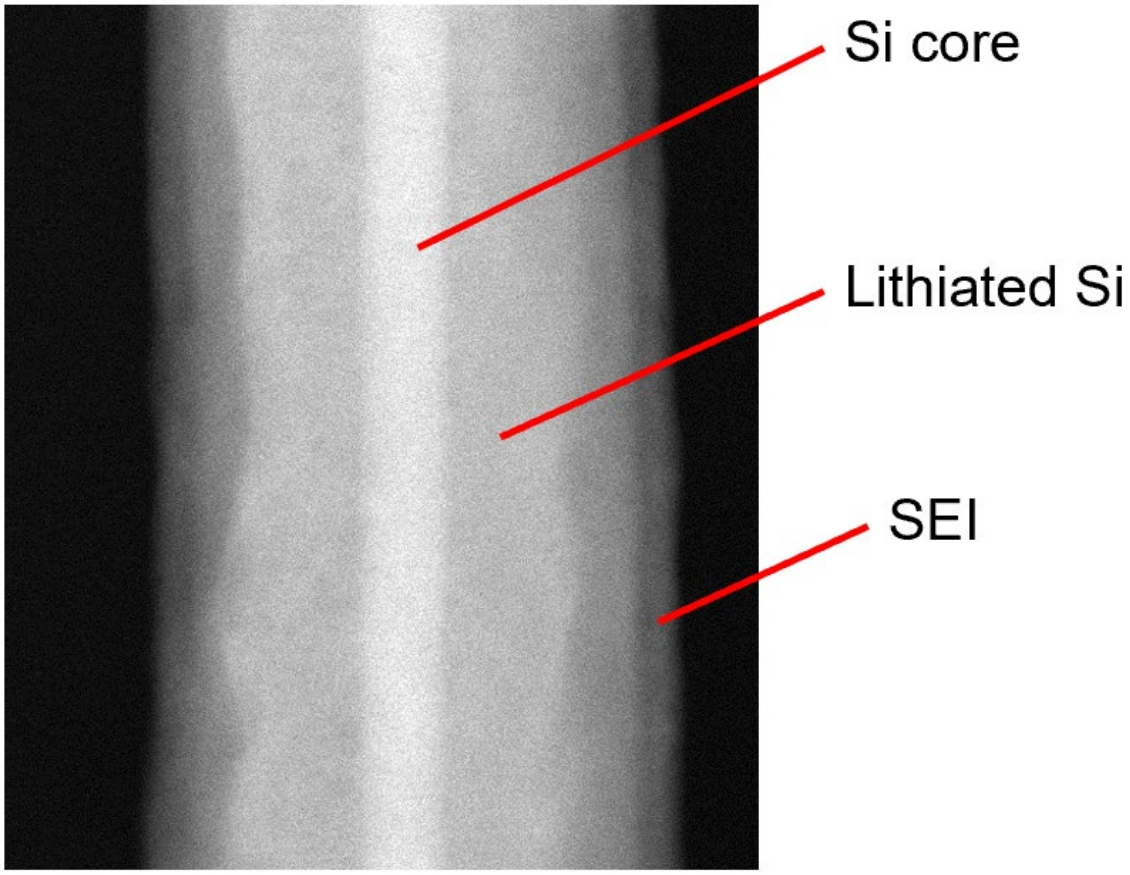

Supplementary Fig. 6 | STEM-HAADF image of a Si nanowire during the 1st lithiation showing the contrasts between pure solid Si core, lithiated Si and the SEI.

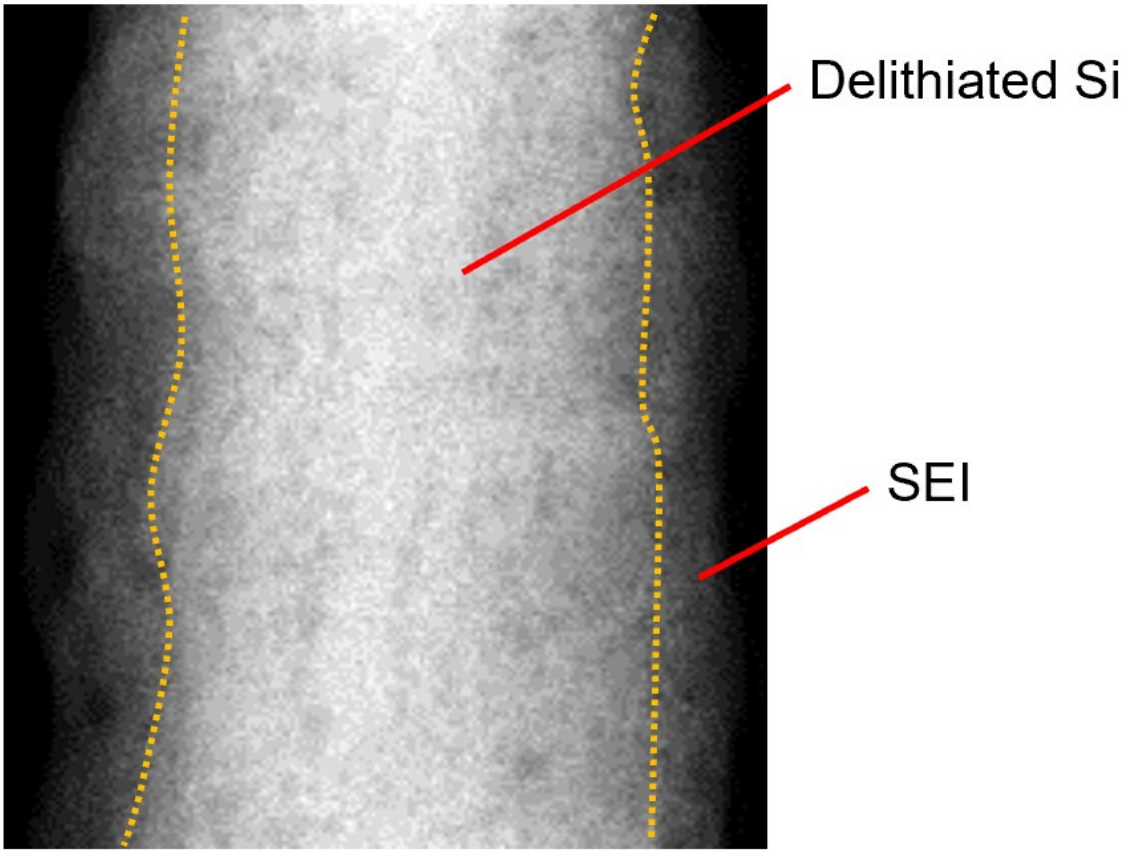

Supplementary Fig. 7 | STEM-HAADF image of a delithiated Si nanowire after 36th cycles.

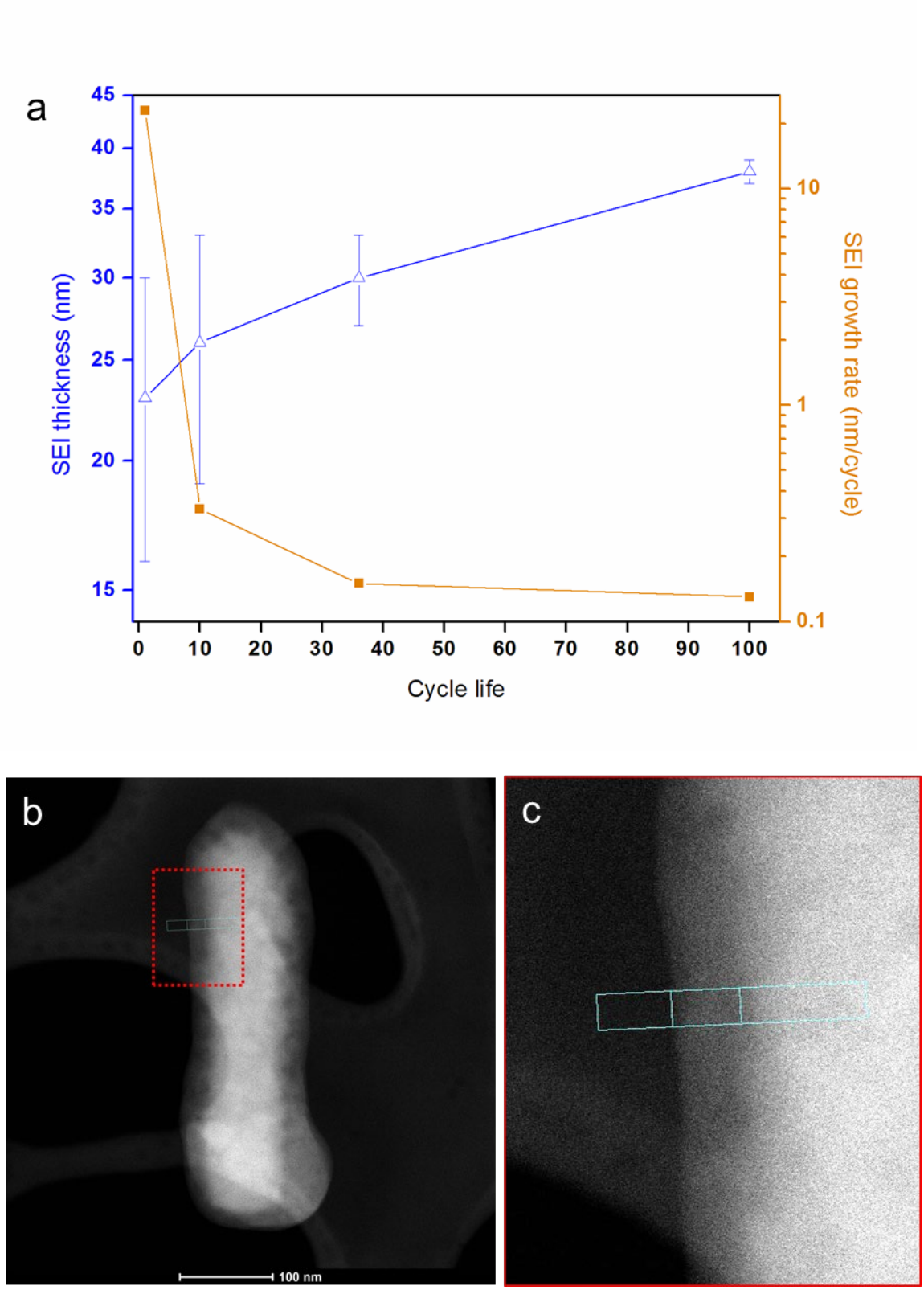
a
SEI thickness (nm)
SEI growth rate (nm/cycle)
Cycle life
45
40
35
30
25
20
15
10
1
0.1
0
10
20
30
40
50
60
70
80
90
100
b
100 nm
c

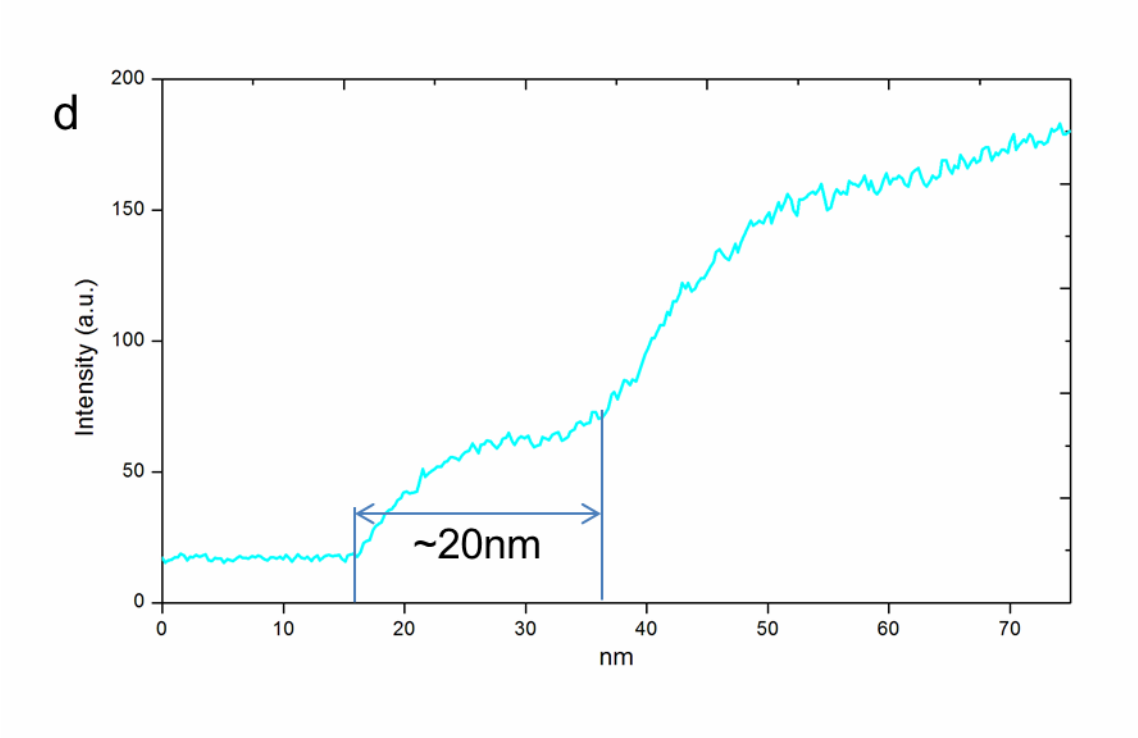

Supplementary Fig. 8 | SEI layer thickness and the growth rate upon cycling of the battery (a). The SEI thickness is directly measured from the STEM-HAADF images of the nanowires. Panel (**b-d**) shows the steps for the measurement. Regions with relatively clear contrast between the SEI and the delithiated Si core are chosen for the measurements, as shown in panel (**b-c**). By using the Digital Micrograph software, the corresponding STEM-HAADF intensity profile can be extracted as shown in panel (**d**). The thickness of the SEI is determined based on the intensity profile and the fact that SEI is relatively lighter than the delithiated Si core. Note that 5 independent measurements at different regions of 3 Si nanowires are used for each SEI thickness evaluation. The measurements here only provide an estimated value of the SEI, since the SEI thickness is not uniform on the Si nanowire surface and ice that is hardly avoidable in the cryo-TEM experiments may present on the Si nanowire (though ice is normally sputtered very quickly upon the zoom-in). The SEI growth rate is calculated by dividing the increment of SEI thickness using the cycle life increment.

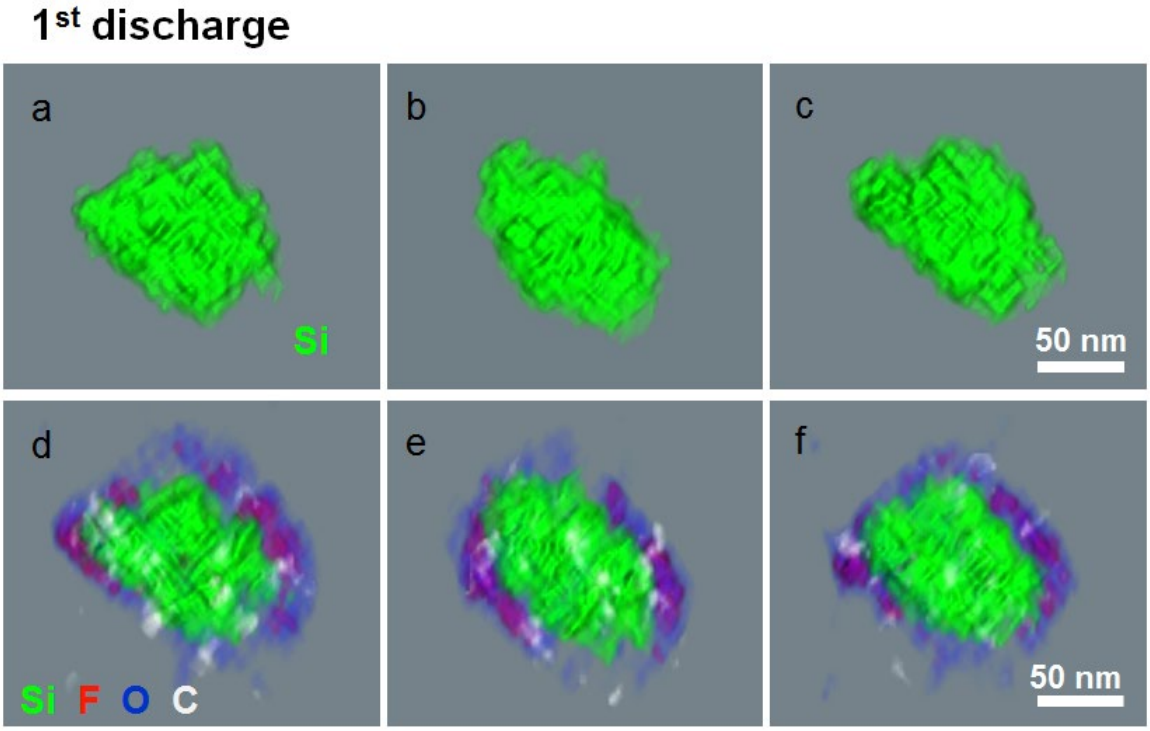

Supplementary Fig. 9 | Additional data showing segmented cross-section views for the 1st cycle nanowire without (a-c) and with (d-f) the SEI. The core is clearly integral. Contrast within the core can be attributed to the mass thickness difference due to the presence of pores within the core. The "core-shell" configuration of SEI/Si is clearly demonstrated. Slice thickness is 5 nm. Each element is color coded. It should be noted that C signal can be detected within the core which we believe is an artifact due to the carbon signals from the lacy carbon of the TEM grid.

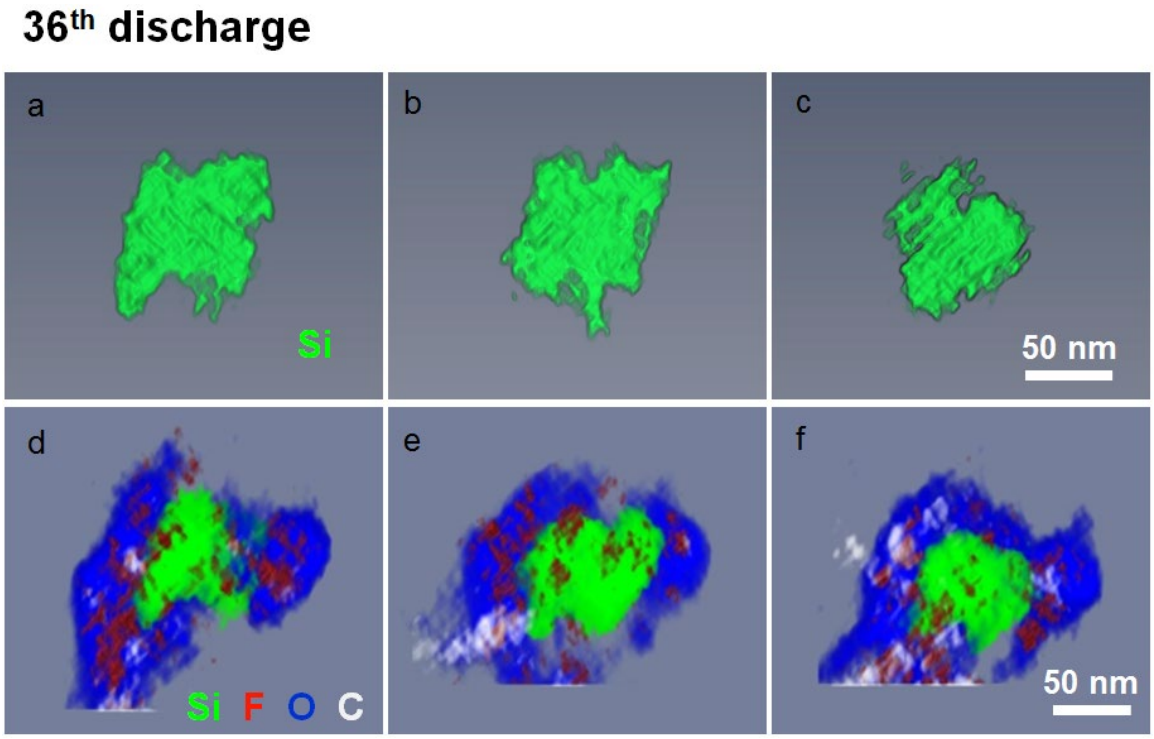

Supplementary Fig. 10 | Additional data showing segmented cross-section views for the 36th cycle nanowire without (a-c) and with (d-f) the SEI. The core is more damaged compared to that of the 1st cycle and remains relatively integral compared to that after 100 cycles (see following), which is consistent with the fact that the capacity retention at this stage is 94.5%. The SEI apparently starts to breach into the Si core, as non-trivial F is detected within the core region (also see Fig. 4b&e in the main text). Slice thickness is 5 nm. Each element is color coded.

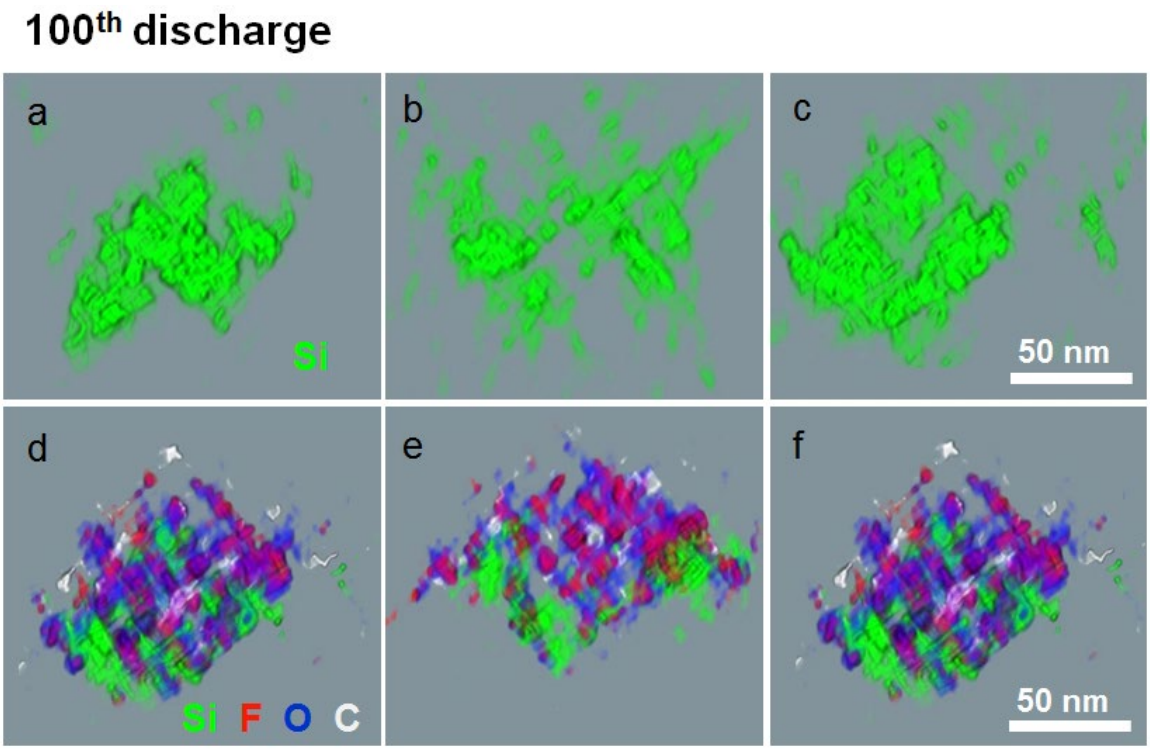

Supplementary Fig. 11 | Additional data showing segmented cross-section views for the 100th cycle nanowire without (a-c) and with (d-f) the SEI. The core is clearly disintegrated. The "core-shell" configuration of SEI/Si is clearly demonstrated. Slice thickness is 5 nm. Each element is color coded.

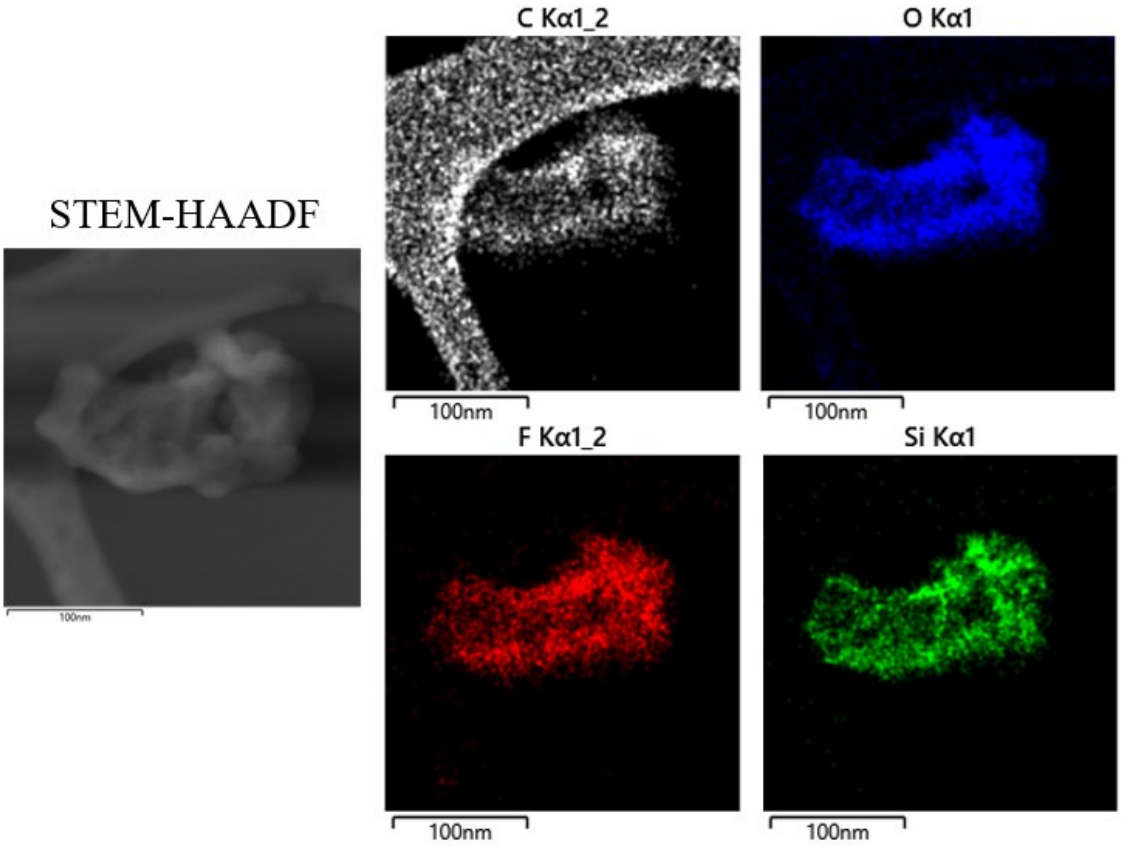

Supplementary Fig. 12 | Cryo-STEM EDS maps of the Si nanowire following 100 cycles at charged state, indicating similar structural feature as the case of discharged state.

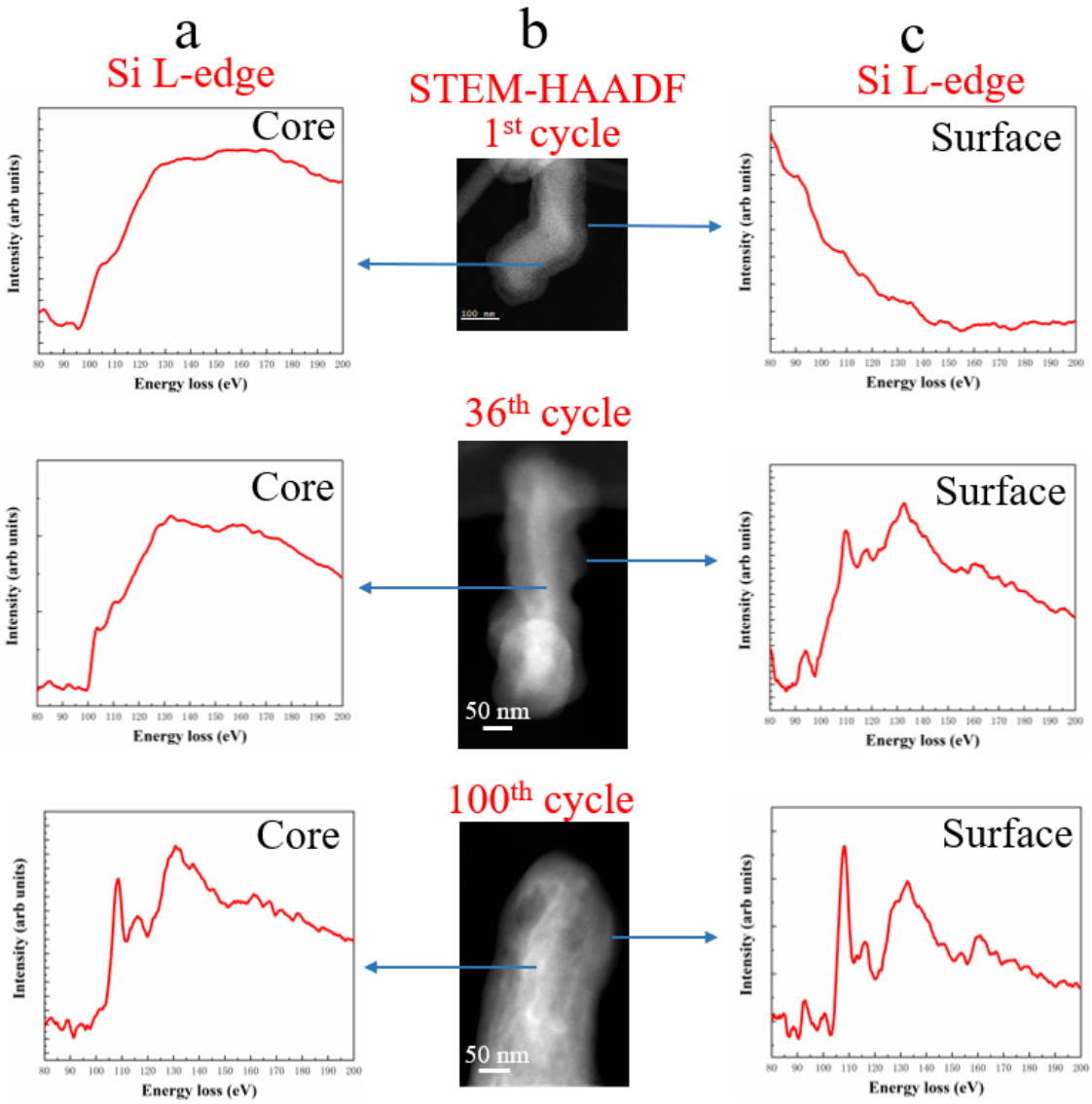

Supplementary Fig. 13 | Comparison of EELS of Si Li-edge of the Si nanowire following different cycles with that of Si and SiO_2. (a) Si L-edge from the core of the Si nanowire following1st, 36th, and 100th cycle. (b) STEM-HAADF image of the Si nanowire following1st, 36th, and 100th cycle. (c) Si L-edge from the surface of the Si nanowire following1st, 36th, and 100th cycle. The EELS indicates that following the 1st cycle, the surface shows no Si, indicating a SEI. With progressive cycling, the growth of SEI toward interior of Si lead to gradual oxidation of Si, especially at the surface.

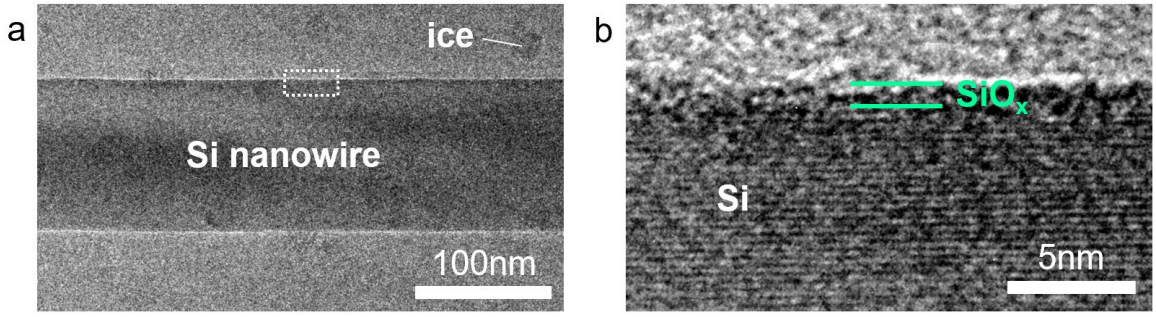

Supplementary Fig. 14 | Cryo-TEM characterization of the pristine Si nanowire. (a) Low magnification of the nanowire showing well-defined surfaces. The nanowire is supported on an amorphous carbon film on the TEM grid. Small ice pieces form due to the condensation of water vapor during the transfer of the cryogenic sample in air. (b) High magnification of the boxed area in panel (a), showing lattice fringes of the pristine crystalline Si nanowire and a thin layer of amorphous oxide on the surface.

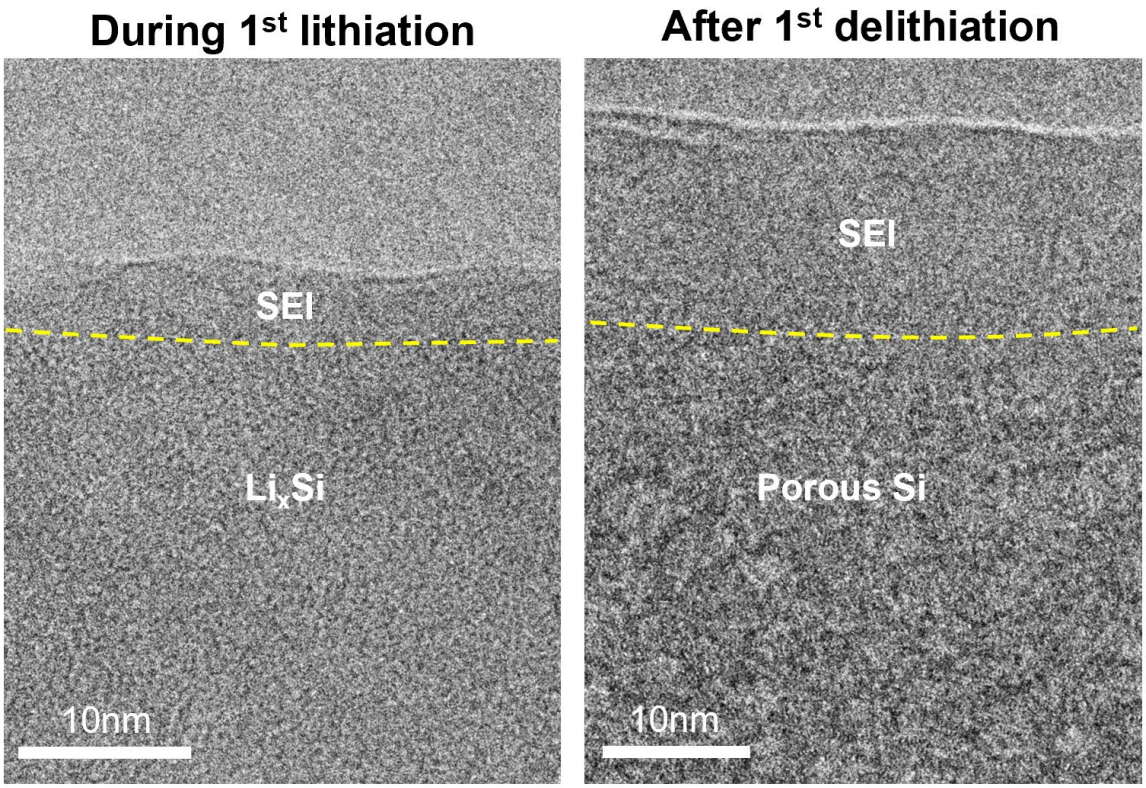

Supplementary Fig. 15 | Cryo-TEM image of the Si nanowire during and after 1st delithiation. Formation of pores ensuing the extraction of Li is clearly demonstrated. Dash line indicates roughly the position of the interface between SEI and the porous Si. Note that the SEI layer thickness measurement from such high resolution cryo-TEM images is not accurate due to the non-trivial electron beam sputtering effect.

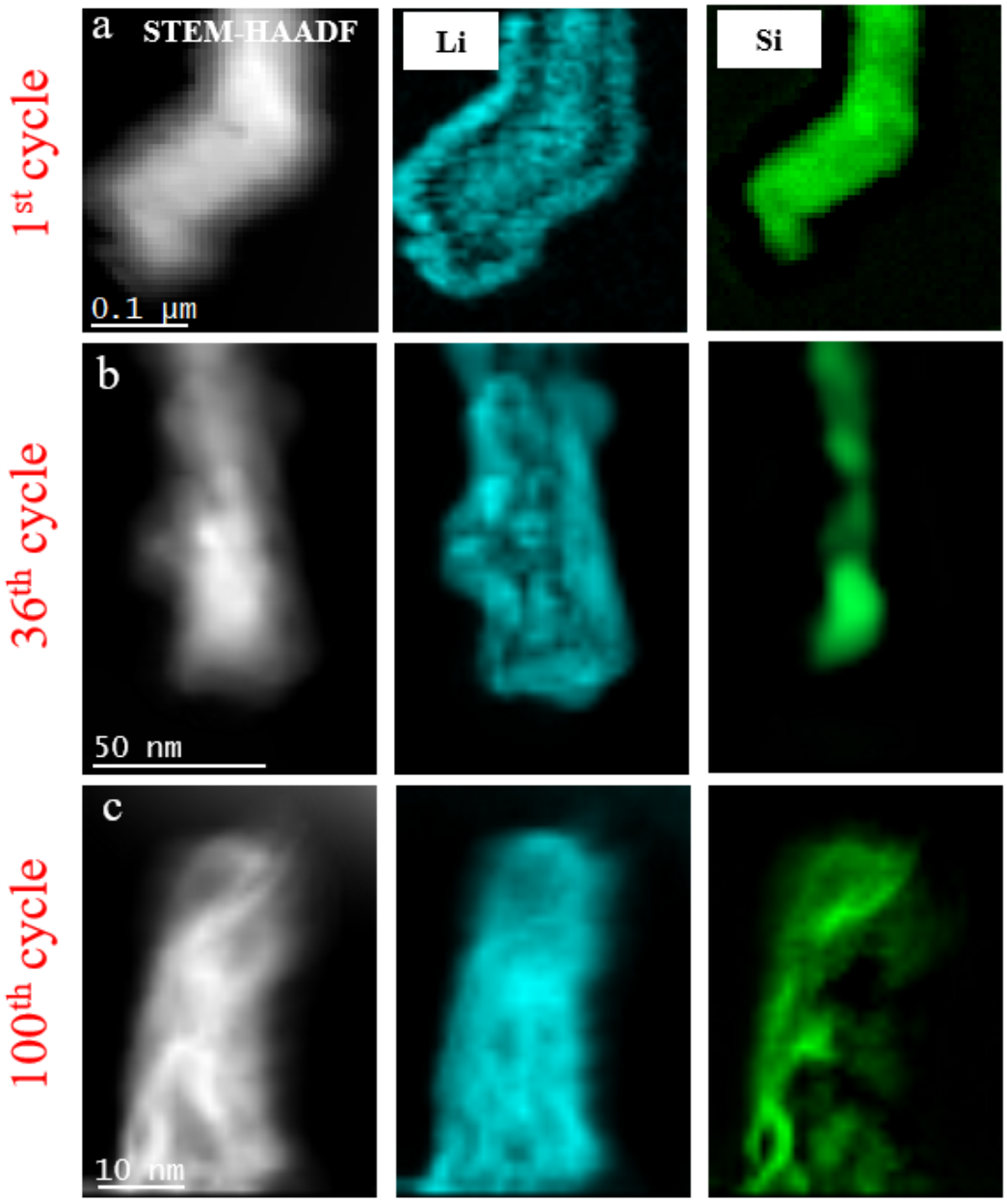

Supplementary Fig. 16 | STEM-HAADF image and Cryo-STEM EELS maps, showing the growth of SEI toward interior of Si leads to the "Li trapping" with gradual increased number of cycling.

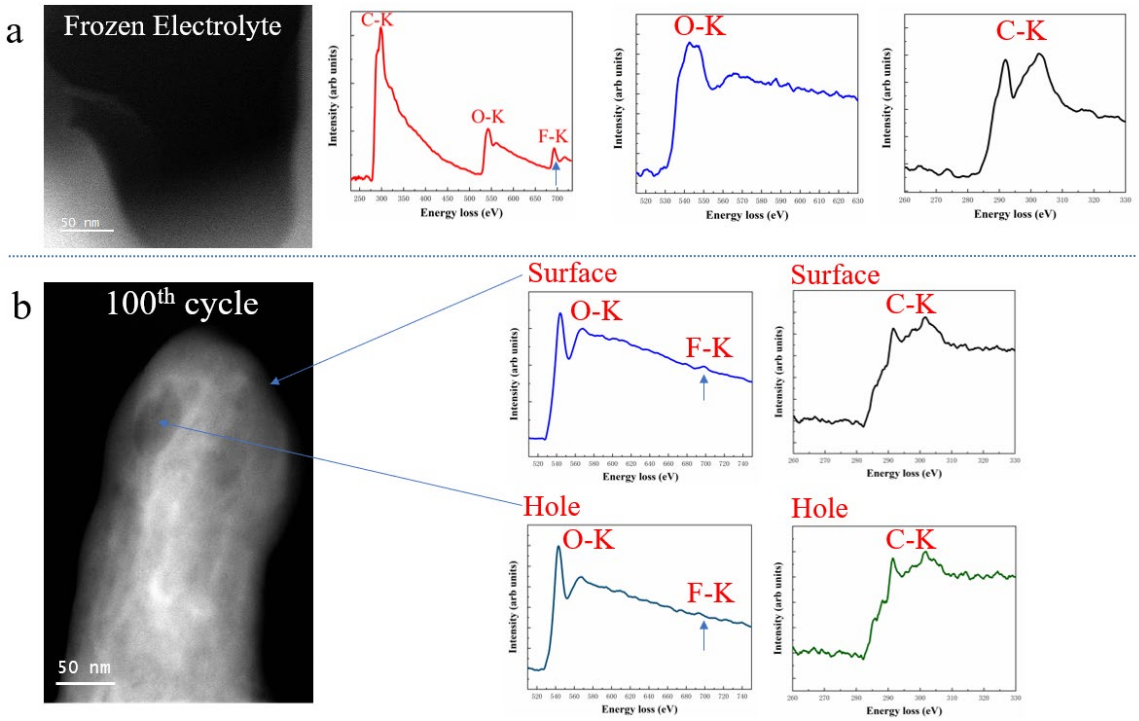

Supplementary Fig. 17 | STEM-HAADF image and cryo-STEM EELS to check if electrolyte is trapped in the void of Si following 100 cycles during the cryo-STEM sample preparation. (a) STEM-HAADF image and EELS of frozen electrolyte, featuring a strong F K-edge. (b) STEM-HAADF image and EELS of Si following 100 cycles, showing no strong F K-edge. Further, the EELS from the pore region is much similar with that from the surface region, consistently indicating SEI growth towards the interior of Si. All these demonstrate that the electrolyte does not trapped into the pore during the sample preparation.

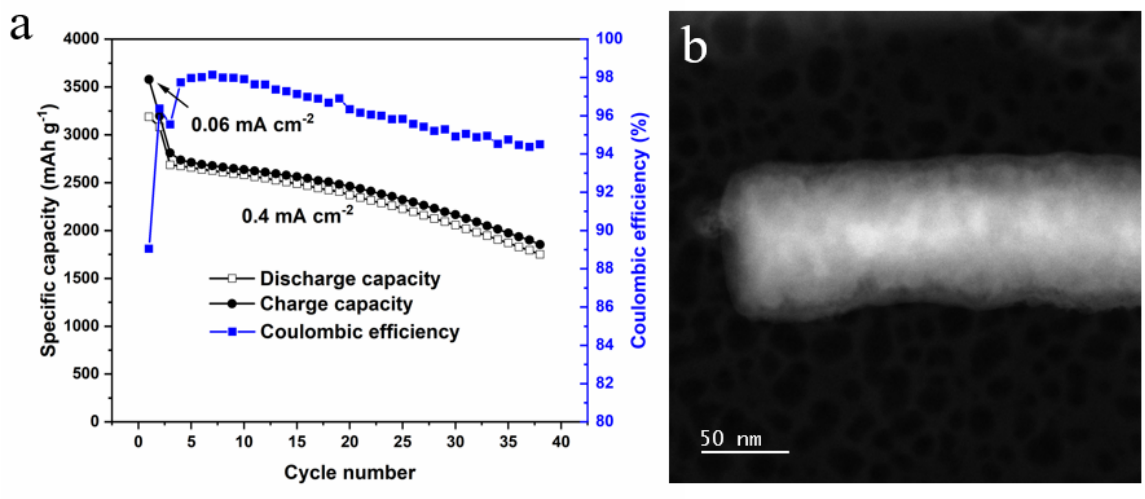

Supplementary Fig. 18 | Electrochemical properties and Cryo-STEM HAADF image of silicon nanowire cycled using electrolyte without FEC. (a) Capacity and Coulombic efficiency as a function of cycle numbers. (b) Cryo-STEM HAADF image showing the fluffy structure following 36 cycles at discharged state.

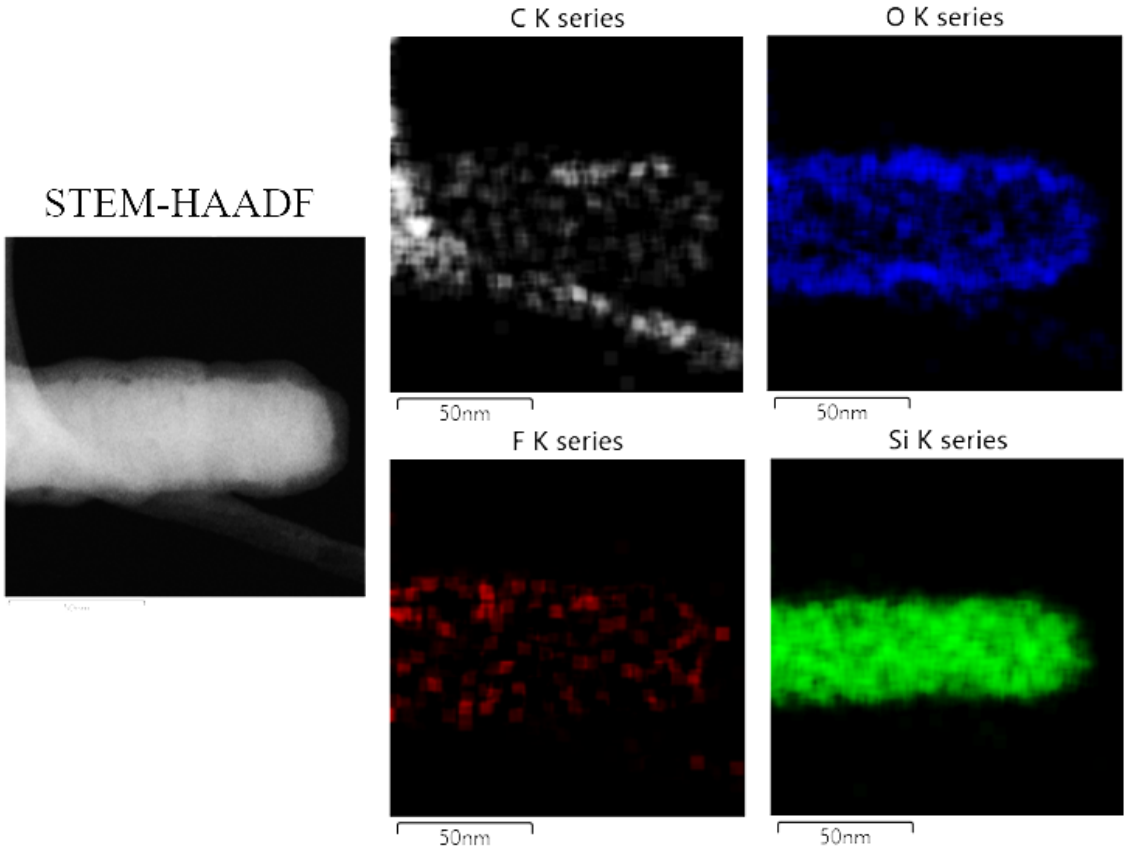

Supplementary Fig. 19 | Cryo-STEM EDS maps of the Si nanowire following 36 cycles at discharged state without FEC additive in the electrolyte, revealing SEI growth towards the interior of Si.

Evaluation of electron beam effect and optimization of imaging condition

To illustrate the beam damage is minimal, supplementary Fig. 20 illustrate the sample before and after the tomographic data acquisition.

The following effort has been made to minimalize the beam damage to the samples.

First, we studied how much irradiation samples can take under cryogenic conditions by varying the beam dose (controlled by beam current and acquiring time). As seen in supplementary Fig. 21, after acquisition with a beam dose of 8.9 $x10^6$ e/nm^2, some beam introduced voids start to form on the wire surface, but most part of SEI layer is still intact since the surface of the nanowire still look smooth. However, after exposure with beam dose over $1x10^7$ e/nm^2, the nanowire got toasted, the surface SEI layer was significantly sputtered, and more pores formed within the SEI and the nanowire. Based on the above facts, for all the tomography acquisition, we keep the total e-beam dose on the samples below $1x10^7$ e/nm^2 to avoid major beam damage. The total beam dose for the EDS tomography acquisition on Si nanowires after the 1st delithiation is 1.97 $x10^6$ e/nm^2. The total beam dose for the EDS tomography acquisition on Si nanowires after the 36th delithiation is 4.3 $x10^6$ e/nm^2. The total beam dose for the EDS tomography acquisition on Si nanowires after the 100th delithiation is 7.7 $x10^6$ e/nm^2.

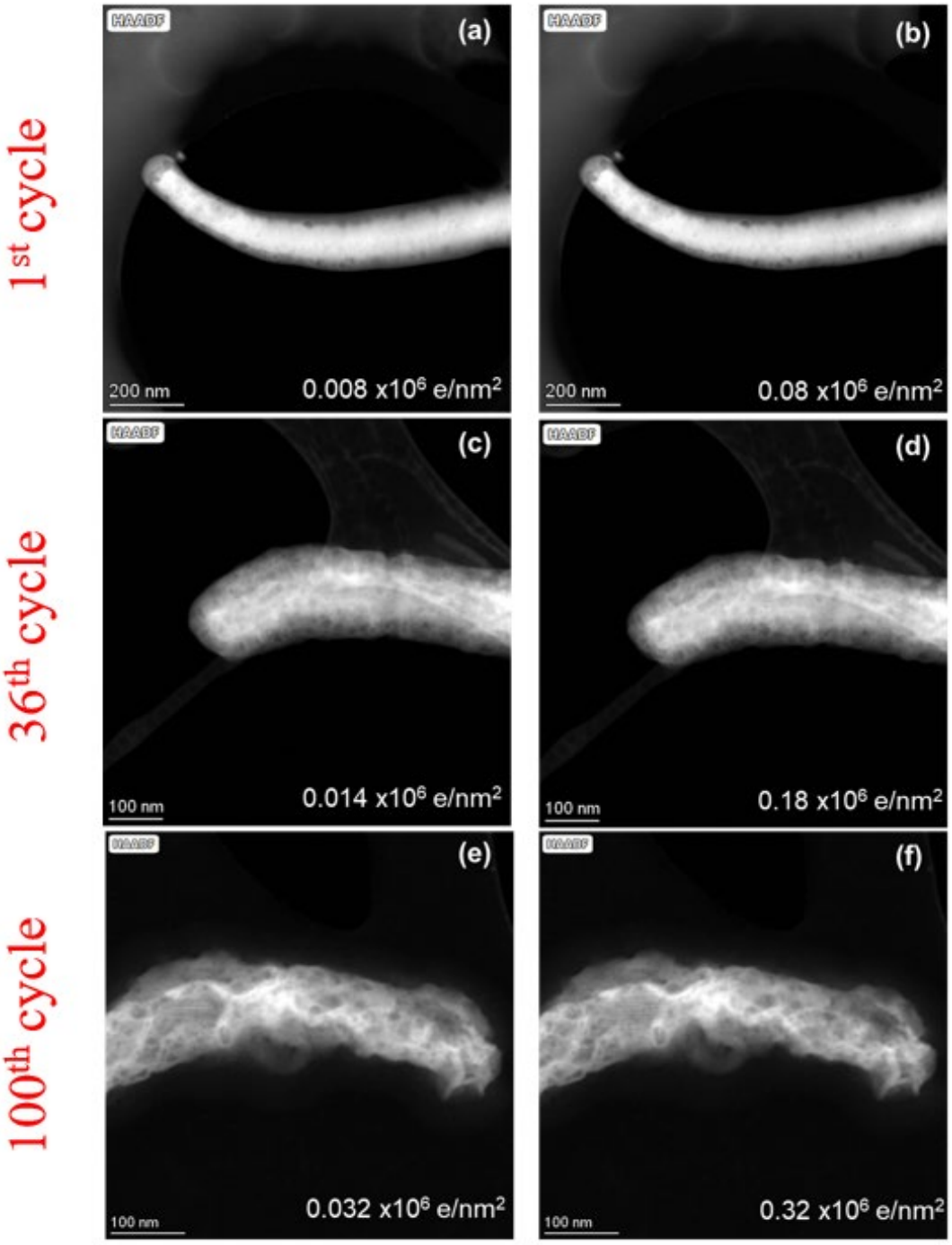

Supplementary Fig. 20 | Comparison of STEM-HAADF image of before and upon EDS tomographic mapping to assess the electron beam effect. a-b. The first (a) STEM image of a Si nanowire after the 1st delithiation and the STEM images of the same nanowire half-way through the EDS tomography (b). **c-d.** The first (c) and the last (d) STEM images acquired in the EDS tomography of a Si nanowire after the 36th delithiation. **e-f.** The first (e) and the last (f) STEM images acquired in the EDS tomography of a Si nanowire after the 100th delithiation.

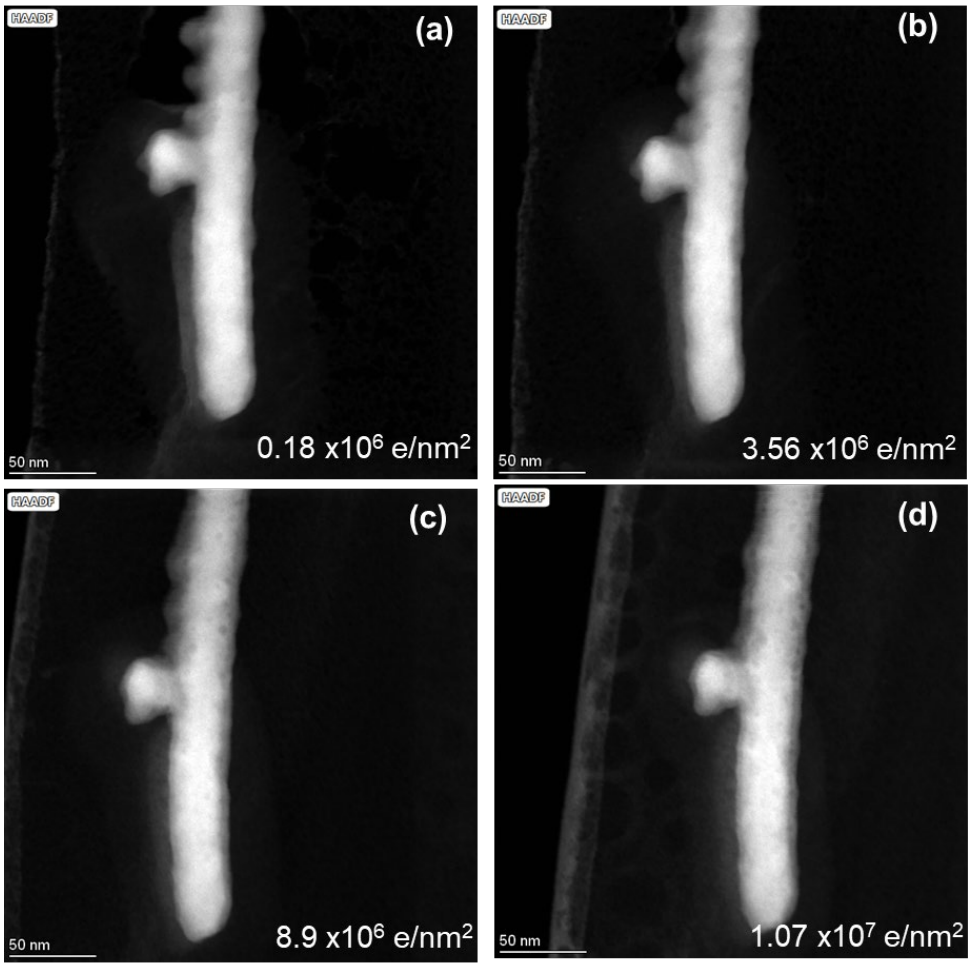

Supplementary Fig. 21 | STEM images of a Si nanowire after the 1st delithiation with different e-beam exposure dose with a probe current of 200 pA to evaluate the beam effect.

Additionally, we employed the following techniques to further minimize the beam damage to our samples during the EDS tomography acquisition.

1) the low-dose acquisition set-up has been utilized. As schematically shown in supplementary Fig. 22, to do tomography acquisition, we normally need to set up a tracking region to bias the drift of the sample and a focus region to set objective lens to desired defocus value at different tilts. Usually, these regions are set-up on the same region as the region of interest. For low-dose acquisition, we do automatic sample tracking and focusing not on the region of interest, but on nearby regions. In this way, we can minimize the beam exposure and thus the damage in the region of interest.

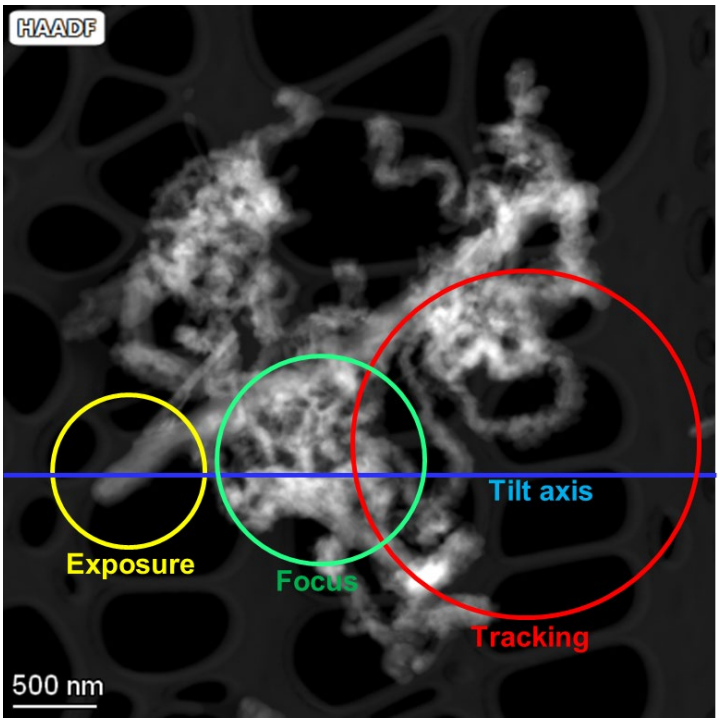

Supplementary Fig. 22 | Schematic to show the low-dose acquisition set-up. The red circle region is for tracking, the green region is for focusing, the yellow region is for the sample region of interest.

2) bidirectional tilt scheme had been employed in the acquisition. The different tilt schemes are shown in the supplementary Fig. 23 and more details can be found in the reference (Turoňová, B. *et al.* Benchmarking tomographic acquisition schemes for high-resolution structural biology. *Nat. Commun.* **11**, 876 (2020)). For bidirectional tilt scheme, the accumulated dose at low tilt angles is smaller compared to that of continuous tilt scheme, thus it provides the higher quality images for 3D reconstruction.

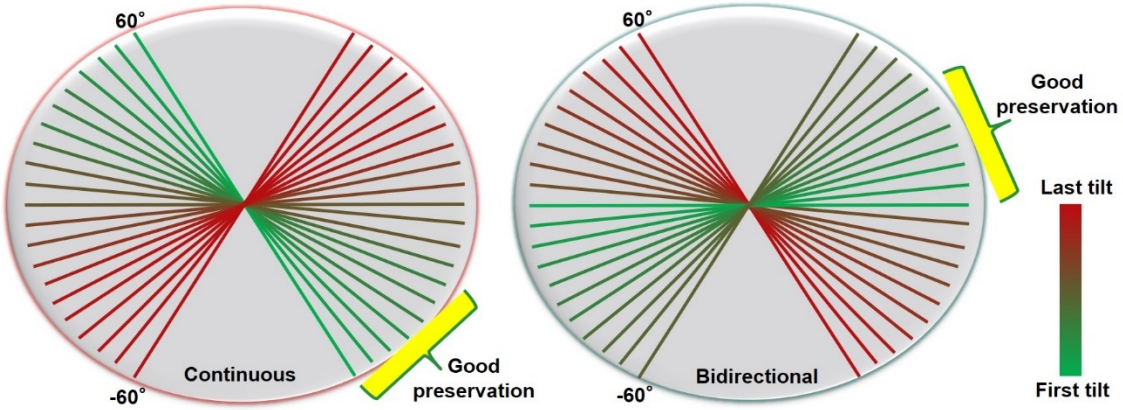

Supplementary Fig. 23 | Schematic to show the tilt scheme during the tomography acquisition.

By employing the advanced techniques as described above, beam-damage to the samples during the EDS tomography acquisition is significantly mitigated. As seen in supplementary Fig. 20, morphology of the Si nanowire looks very similar before and after the EDS tomography acquisition.

We studied beam dose effects on EDS signal and radiation damage, to determine the optimal dose and minimize radiation damage while maintaining required counts for reconstruction. Obviously, higher beam dose means more EDS signal for the reconstruction, but more radiation damage. The beam dose can be controlled by probe current and total acquiring time. We controlled the beam current at a range from 150 pA to 250 pA, since this is an empirical value for getting good EDS signal for beam-sensitive samples. We varied the total acquiring time and characterized the beam damage based on the HAADF morphologies with different beam dose exposure, as seen in supplementary Fig. 21. In this way, we can determine the total acquiring time of tilt series for avoiding a major beam damage. For example, after exposure to beam dose 8.9 x 10^6 e/nm^2, the sample start to get some damage, as seen in supplementary Fig. 21. We then kept the total acquiring beam dose for sample exposure to beam below this value. The total beam dose for the EDS tomography acquisition on Si nanowires after the 1st delithiation is 1.97 x10^6 e/nm^2. The total beam dose for the EDS tomography acquisition on Si nanowires after the 36 th delithiation is 4.3 x10^6 e/nm^2. The total beam dose for the EDS tomography acquisition on Si nanowires after the 100th delithiation is 7.7 x10^6 e/nm^2.

On the other hand, we studied how much acquisition time per tilt step we need to get enough signal for EDS quantification. As seen in supplementary Fig.24, after 100 s mapping time, the weight percentage of Si becomes stable with increasing mapping time.

Thus, to get reliable quantification result at each tilt, the minimum mapping time is at least 100 second.

Finally, the optimized time we found in our case is 114 s per tilt step, that is 45 mins in total acquiring time. With that mapping time, the Si counts approach 1000 at each tilt step as seen in supplementary Fig. 25, which is enough for EDS tomography reconstruction. The total dose of the Si nanowire undergoing throughout the tomography was 1.97 x 10^6 e/nm^2. With this optimal dose, we can avoid major beam damage and get enough counts for EDS quantification and reconstruction.

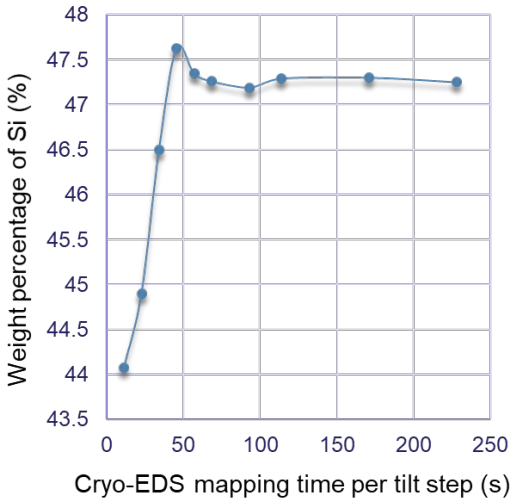

Supplementary Fig. 24 | Si element quantification result with increasing mapping time.

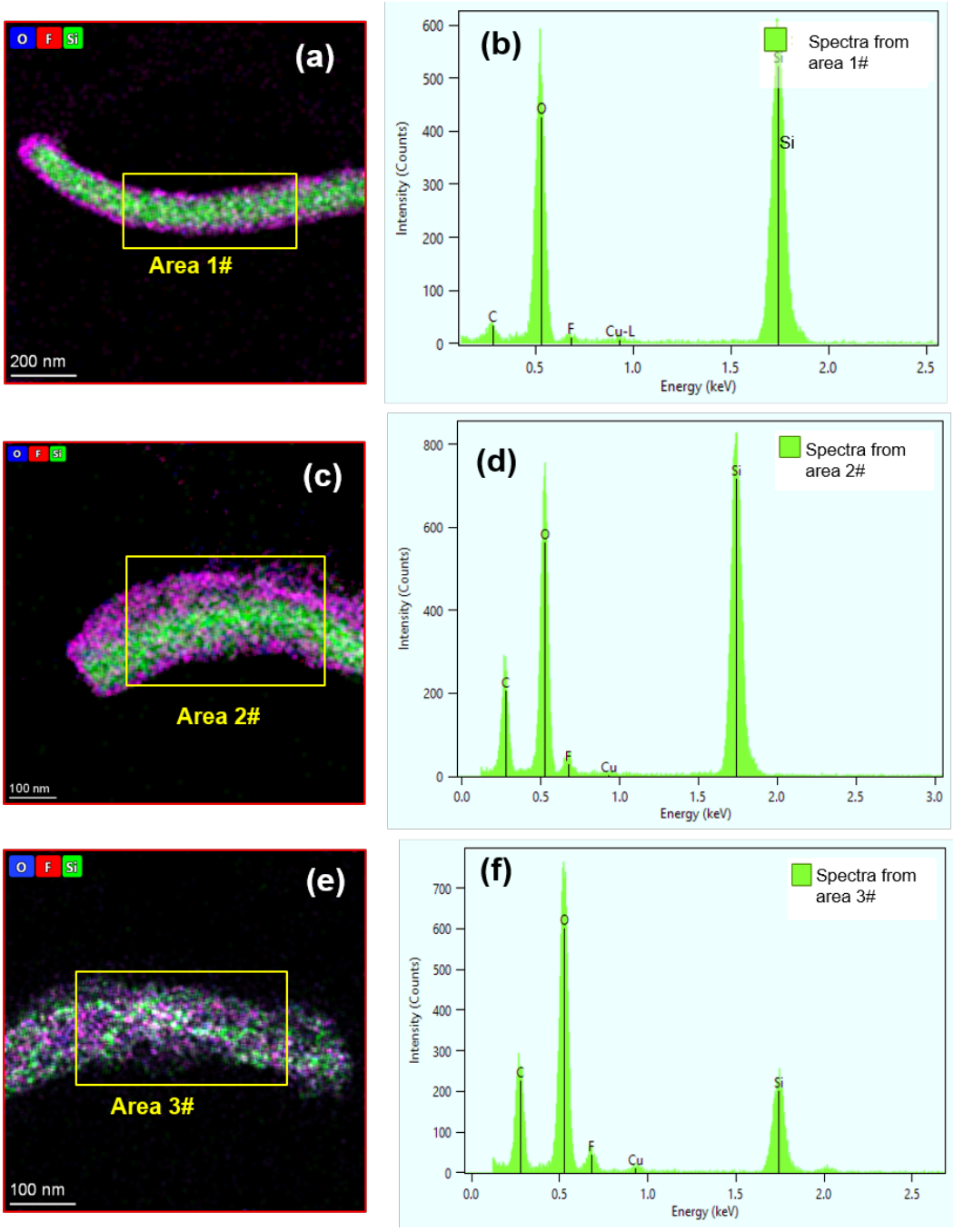

Supplementary Fig. 25 | EDS result of Si nanowires after different cycles. (a) elemental mapping and (b) corresponding spectrum of a Si nanowire after the 1st delithiation cycle; (c) elemental mapping and (d) corresponding spectrum of a Si nanowire after the 36th delithiation cycle; (e) elemental mapping and (f) corresponding spectrum of a Si nanowire after the 100th delithiation cycle. The background was subtracted using multi-polynomial model. The average filter (Kernel size 5 pixels) was applied for the maps to make elements more visible. (Note the peak at ~ 2 keV in (f) corresponds to P, which is a component of SEI layer).

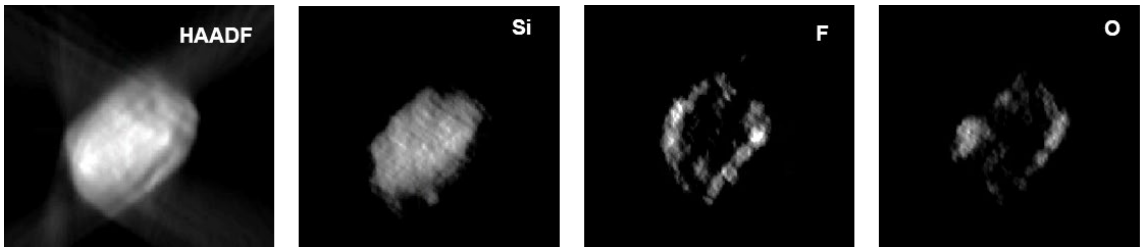

Supplementary Fig. 26 | Representative raw slices of cross sections of a Si nanowire after the 1st delithiation in the HAADF, Si, F and O reconstructions.

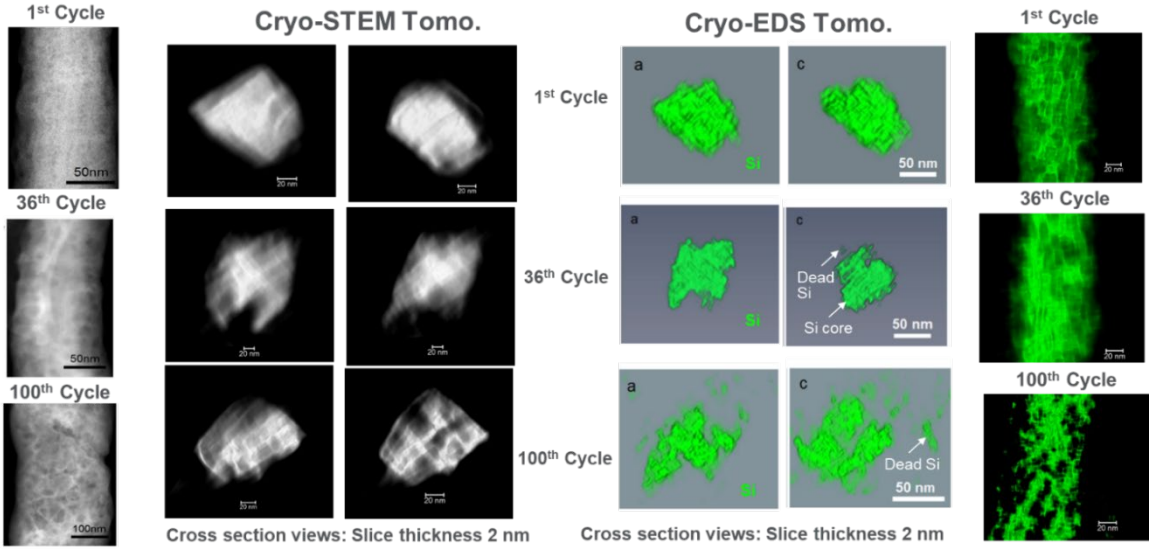

Supplementary Fig. 27 | Comparison of Cryo-STEM tomography with Cryo-EDS tomography results.

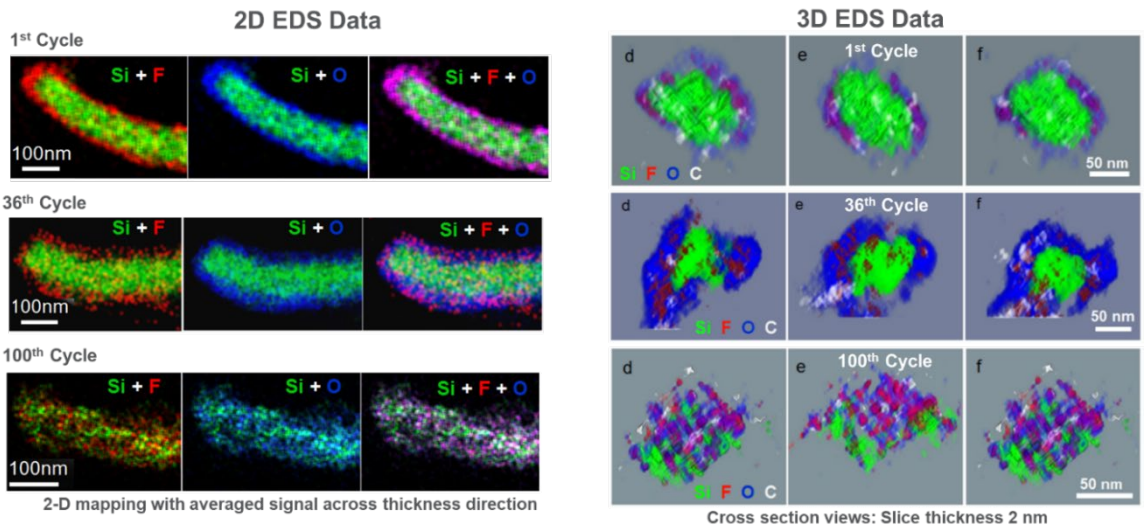

Supplementary Fig. 28 | Comparison of 2D EDS maps with 3D EDS tomography results.

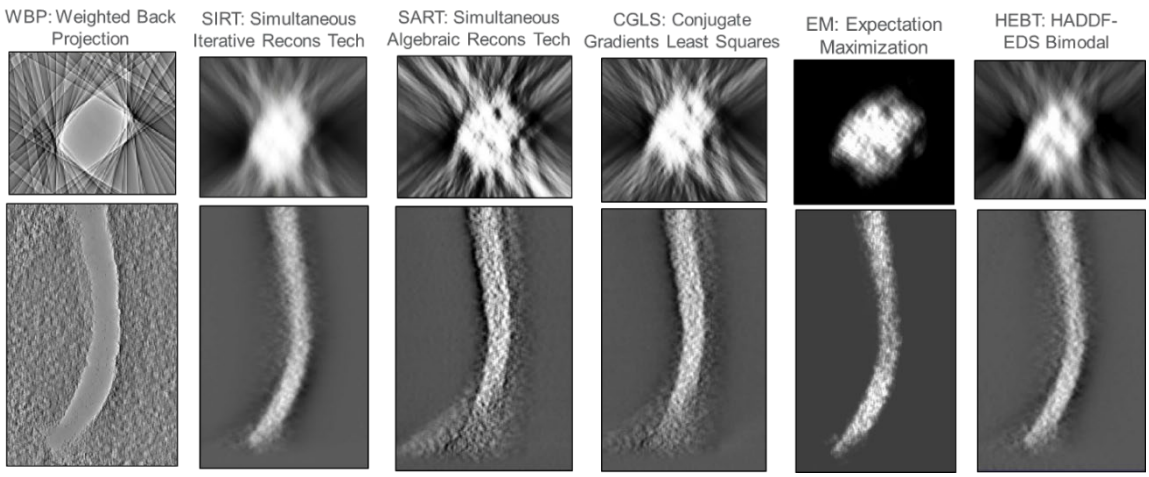

Supplementary Fig. 29 | Compassion of Si (Net EDS counts) reconstruction slices using different algorithms in Inspect 3D. The advantage of using Expectation-Maximization is that it reduces the elongation of particles and dampens more missing wedge artifacts. In statistics, the Expectation-Maximization algorithm is an iterative method to find (local) maximum likelihood or maximum a posteriori (MAP) estimates of parameters in statistical models, where the model depends on unobserved latent variables (Sigworth, F. J., Doerschuk, P. C., Carazo, J.-M. & Scheres, S. H. W. An introduction to maximum-likelihood methods in cryo-EM. *Methods Enzymol.* **482**, 263-294 (2010)). Expectation-Maximization is more or less like simultaneous iterative reconstruction technique (SIRT) and it is actually also known as multiplicative SIRT (as opposed to the additive SIRT).

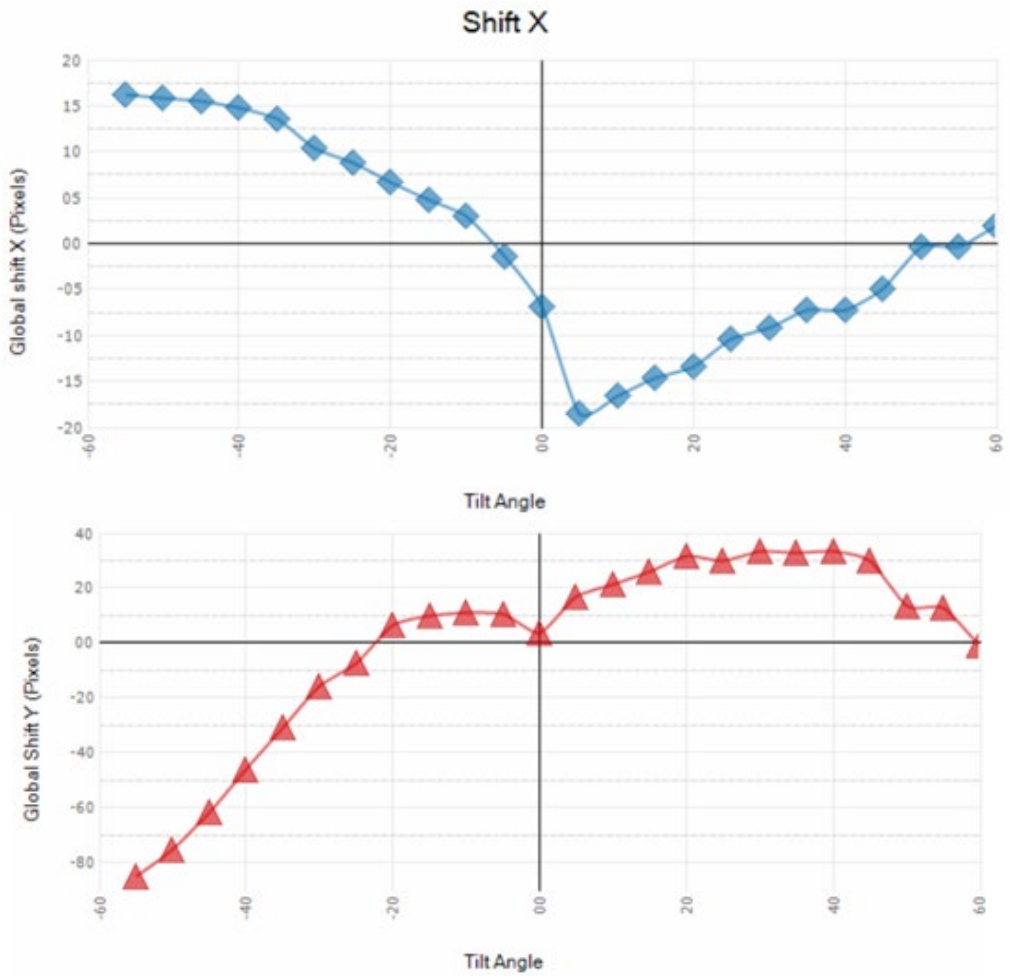

Supplementary Fig. 30 | A typical shift X and shift Y data after the stack alignment for tilt series. Each pixel is equal to 2.13 nm.

Additional information about the background and signal intensity

For spectrum processing, a multi-polynomial model was used for the background correction. The energy peak used for Si fitting is 1.7397 keV; for O fitting is 524.9 eV; for F fitting is 676.8 eV; for C fitting is 277.4 eV. As a representative case, the Supplementary Fig. 31 shows the raw spectrum overlayed with the spectrum after the background subjection (the dark outline).

The spectrum shown in the Supplementary Figure 25 is fitted to derive the peak to background (P/B) ratio, which is conveniently defined as ratio of the net counts at the energy window of a specific element divided by the background counts at the same energy window of that specific element. The net count for Si is located at the energy window from 1.662 keV to 1.818 keV; for O 461eV to 587 eV; for F 626 eV to 726 eV; and for C 231 eV to 321 eV. For the sample of 1st cycle: the calculated P/B ratio is 2.9 for F; 75 for O; 62.4 for Si; and 11.6 for C. For the sample of 36th cycles: the calculated P/B is 4.6 for F; 51.5 for O; 51.3 for Si; and 37.7 for C. For the sample of 100th cycles: The calculated P/B ratio is 25.2 for F; 288 for O; 73.5 for Si; and 195 for C.

All the EDS maps inputted for the reconstruction were background subtracted.

One of the fundamental concerns for the EDS tomography is the weak signal, consequently limiting the attainable resolution. Therefore, it is important that the peak of the element in concern can be identified. To illustrate this, the as-acquired spectrum counts per pixel are provided in supplementary **Figs. 32**, **33** and **34**. As shown in the colored mappings and the extracted spectrums at typical 1x1 pixel regions in the supplementary **Figs. 32**, **33**, and **34**, we can clearly locate the elements in concern.

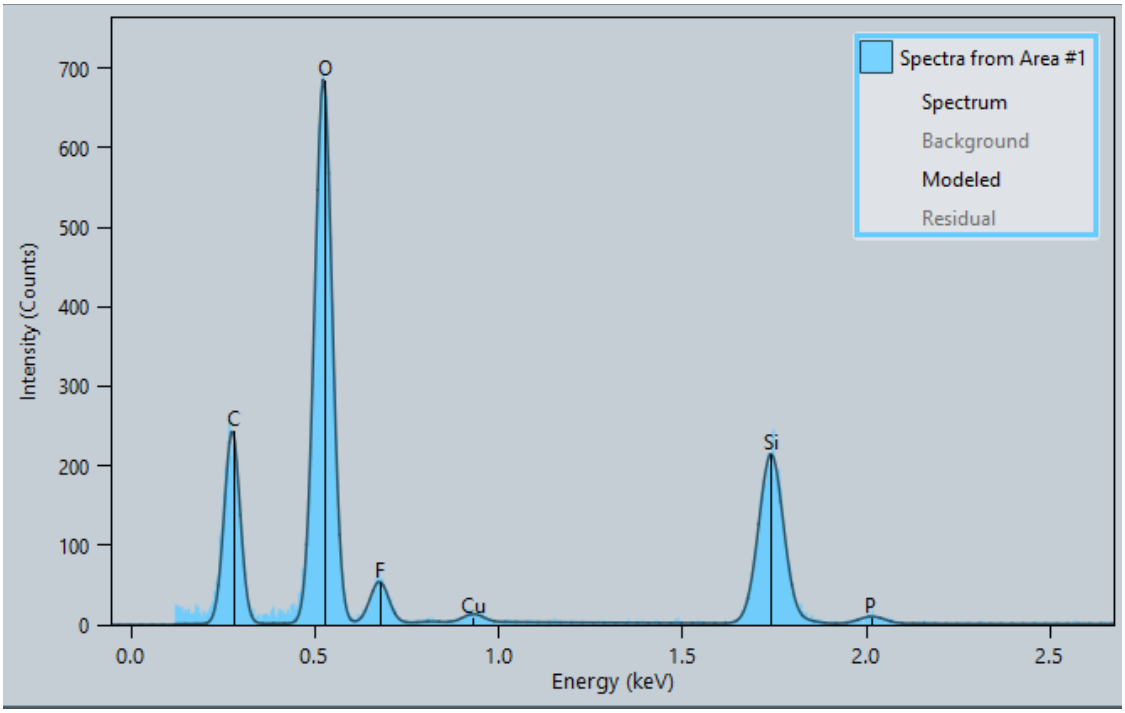

Supplementary Fig. 31. Spectrum background subtraction. The spectrum from the sample of 100th cycles. The blue area is the raw spectrum. The multi-polynomial model was used for the background correction, leading to the background corrected spectrum shown by the dark line. The energy peak used for Si fitting is 1.7397 keV; for O fitting is 524.9 eV; for F fitting is 676.8 eV; for C fitting is 277.4 eV.

To further vividly demonstrate the data quality, we show the spectrum collected from the nanowire and that collected from the supporting carbon film (pixel point #5 in supplementary **Figs. 32, 33, and 34**), demonstrating that the EDS signals of the element in concern at each single pixel region on the nanowire can be seen. It is apparent that elements O, F related to SEI are indeed present in the interior of the Si nanowire after the 100th cycle; and as for nanowires after the 1st cycle, these elements of SEI only present on the surface of the Si nanowire. In other words, the key finding of our work, that is the "SEI inward growth towards the interior of Si", is well substantiated by our Cryo-EDS-Tomography.

To illustrate how much signal is spread in the maps, especially for the case of F as representative case, we show the intensity distribution at each pixel in the supplementary **Fig**. **35** and **Fig. 36** for the case of 1st cycle and 36 cycles respectively. Apparently, at each pixel the count for F is above the background.

Further, we show the spectrum in the feature of 5x5 pixels as Supplementary **Fig. 37**, where all the elements can be clearly identified, even including the peak of P at the energy position of ~ 2 keV, which is a component of SEI and is apparently visible following the 100th cycles.

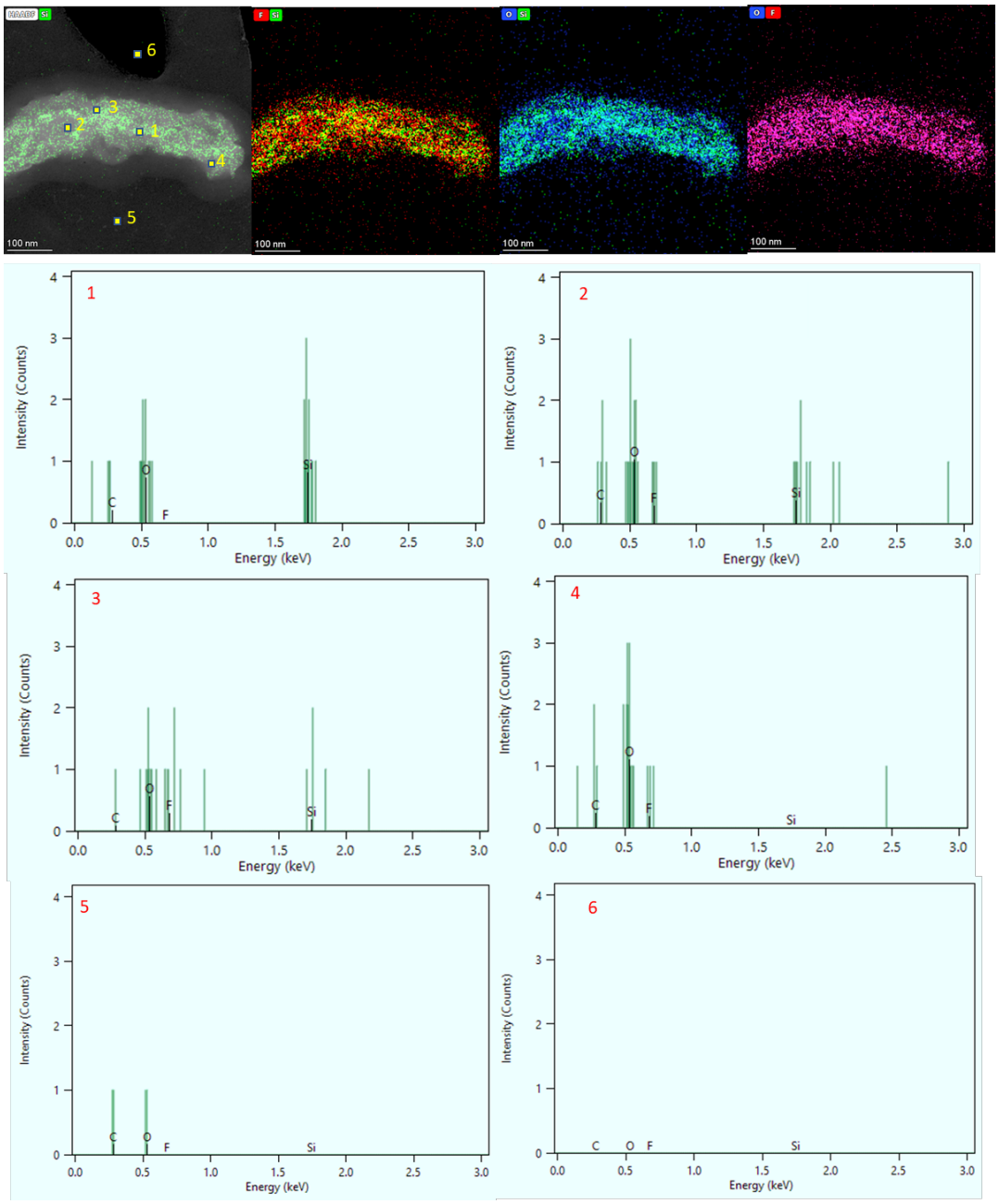

Supplementary Fig. 32 | The spectrum extracted from 1x1 pixel region (pixel size 1.068 nm) at different locations for the sample following 100th cycle. All the spectra were extracted from 2D mapping at each tilt angle, and they were not from reconstruction tomography. By comparison of the spectrum at different pixels, we can tell the distribution of elements. It should be noted that in the spectrum2, the counts at ~ 2 keV corresponds to P, which exists in the SEI layer following 100th cycles.

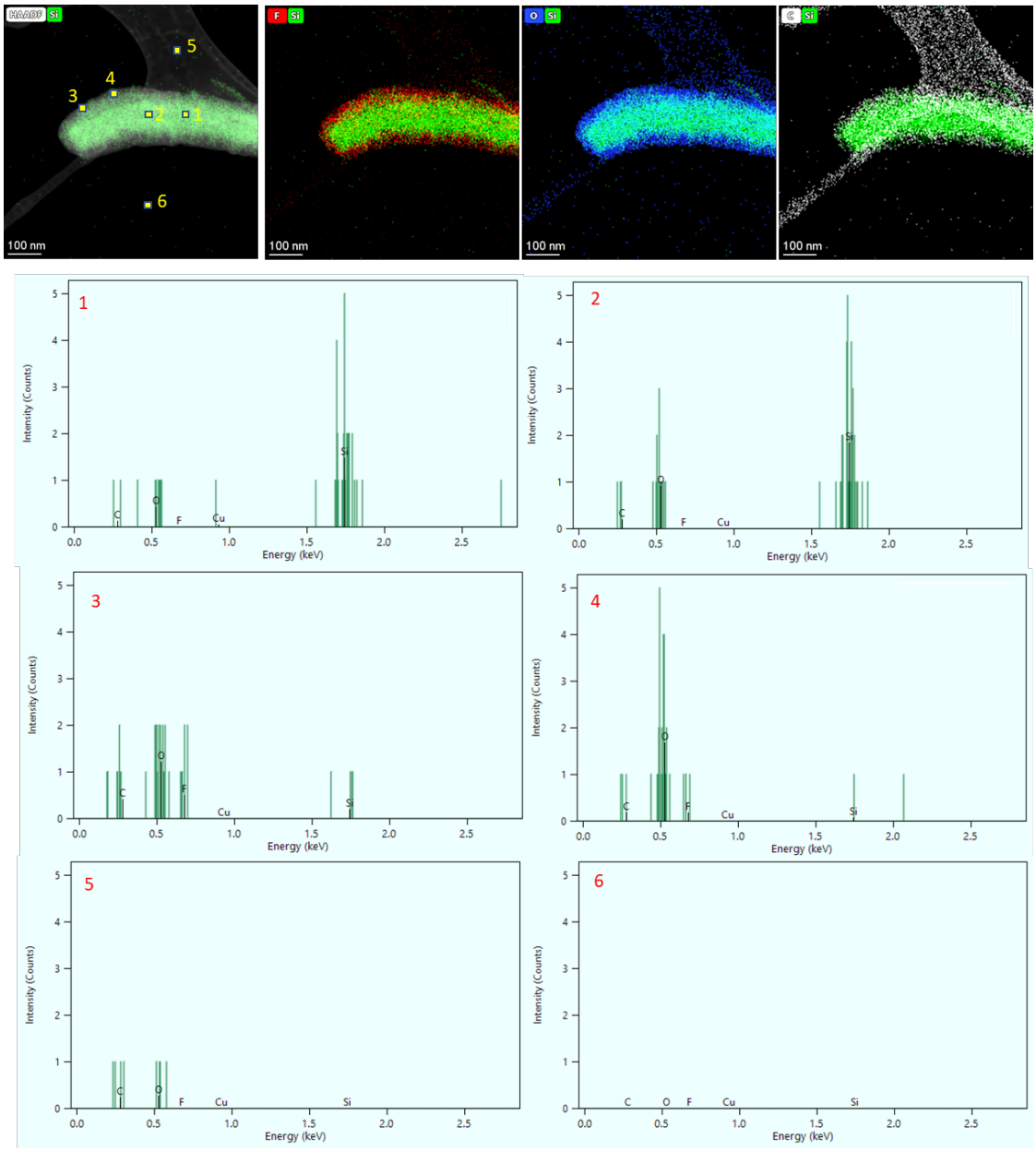

Supplementary Fig. 33 | The spectrum extracted from 1x1 pixel regions (pixel size 1.48 nm) at different locations for the sample following 36th cycle. All the spectra were extracted from 2D mapping at each tilt angle, and they were not from reconstruction tomography. By comparison of the spectrum at different pixels, we can tell the distribution of elements.

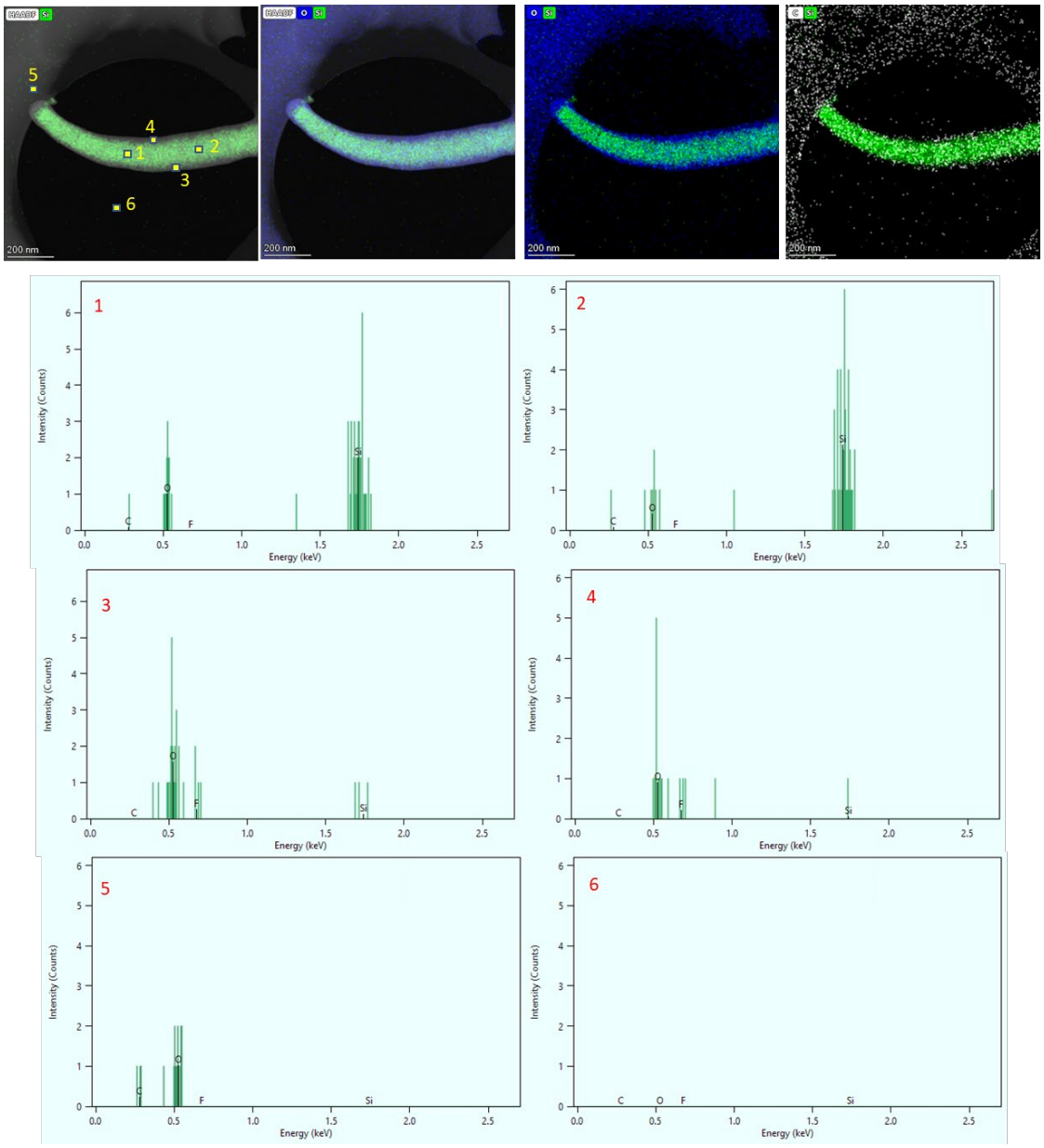

Supplementary Fig. 34 | The spectrum extracted from 1x1 pixel regions (pixel size 2.134 nm) for the sample following 1st cycle. All the spectra were extracted from 2D mapping at each tilt angle, and they were not from reconstruction tomography. By comparison of the spectrums at different pixels, we can tell the distribution of elements.

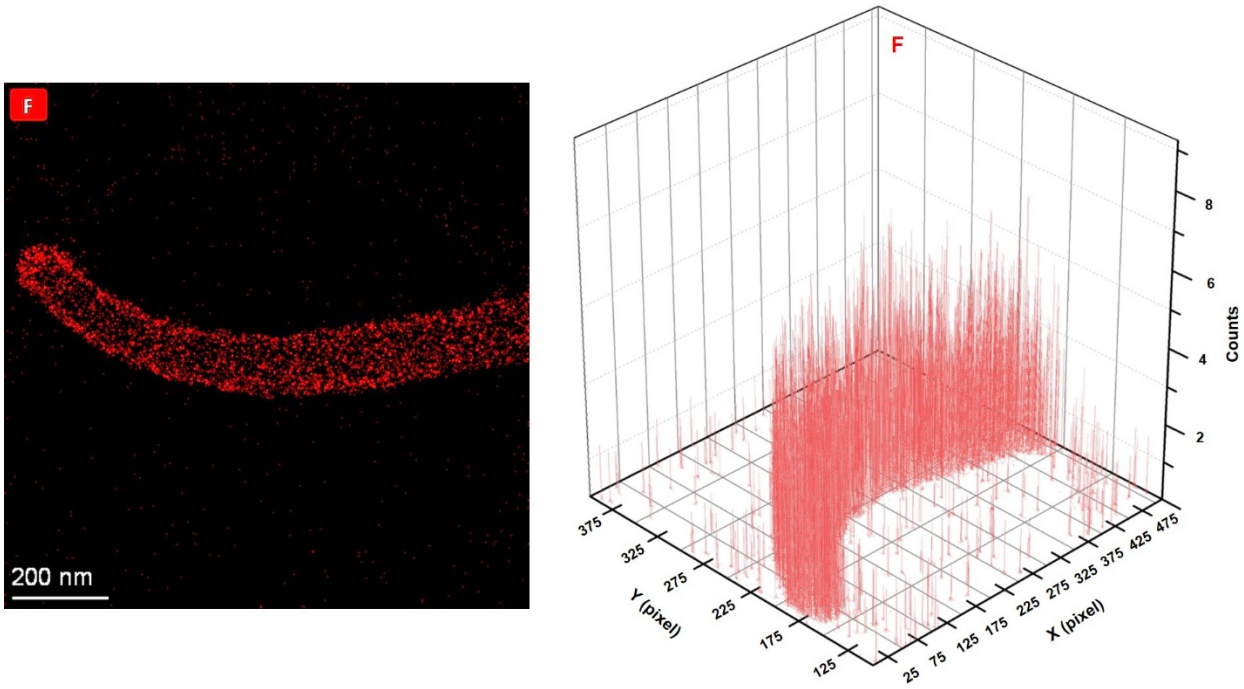

Supplementary Fig. 35 | F Count distribution at 1x1 pixel for the sample following 1st cycle. The left panel is the 2D map of F distribution. The right panel is the F count distribution at each pixel as captured spectrum, illustrating the counts distribution at each pixel for F.

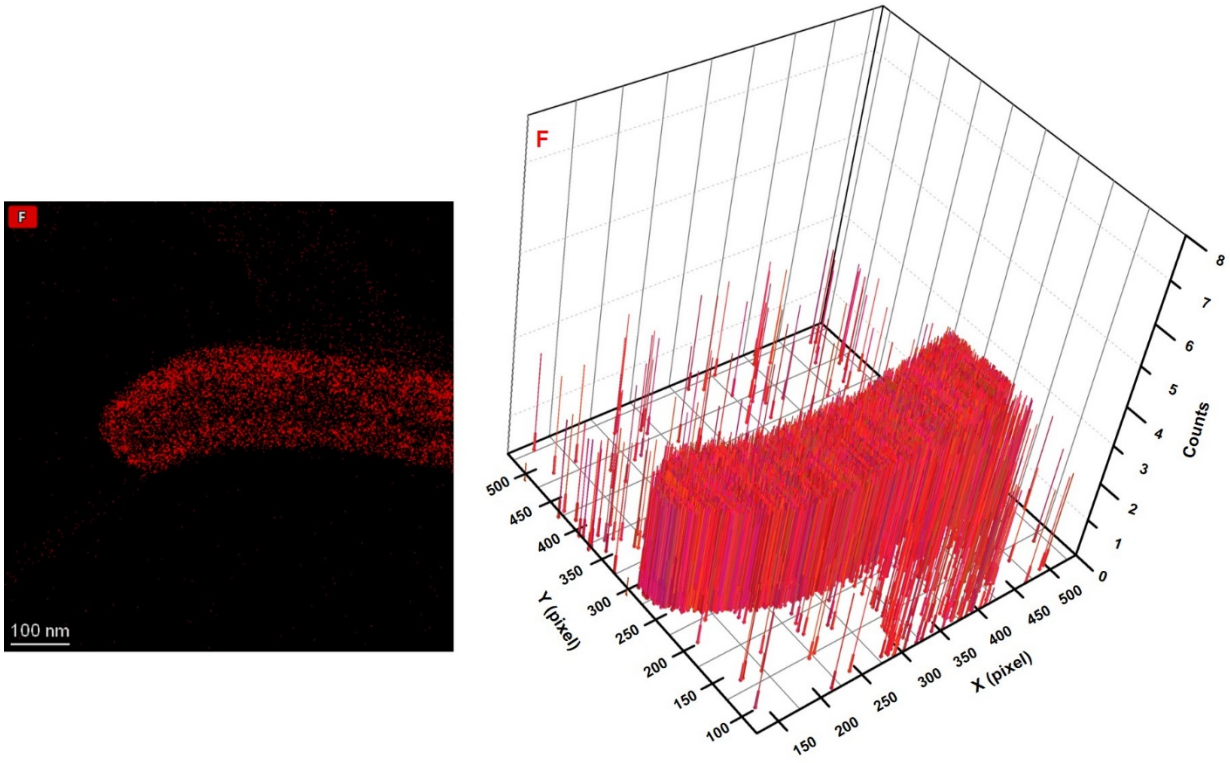

Supplementary Fig. 36 | F Count distribution at 1x1 pixel for the sample following 36th cycle. The left panel is the 2D map of F distribution, right is the F count distribution at each pixel as captured spectrum, illustrating the counts distribution at each pixel for F.

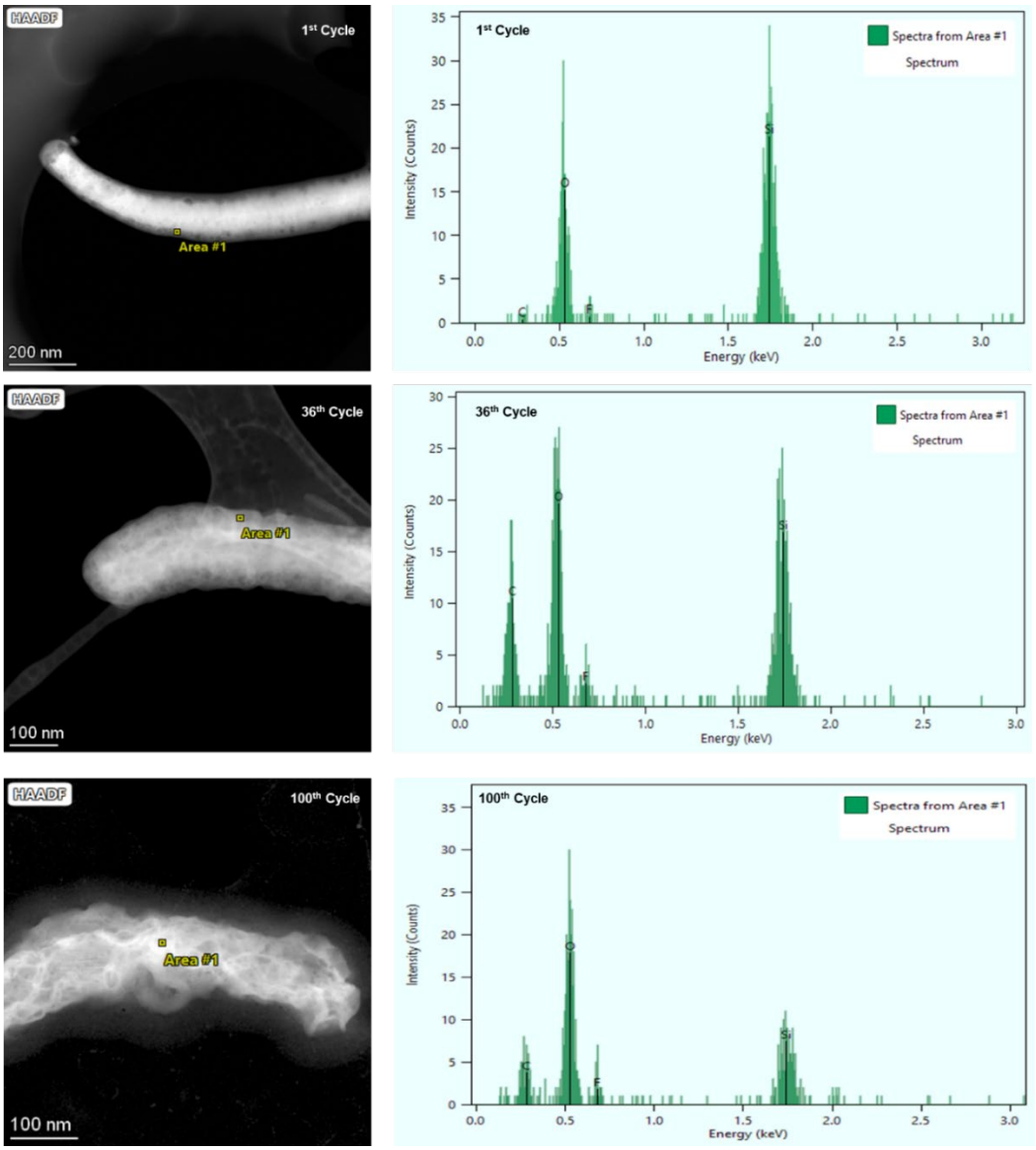

Supplementary Fig. 37 | The spectrums from typical small feature regions (5x5 pixels) to show the counts with each element. The top panel is the 1st cycle; The middle panel is the 36th cycle; and the bottom panel is the 100th cycle. Note the peak at ~ 2 keV corresponds to P, which is a component of SEI layer and is detected following the 100th cycling.

Supplementary Discussion

Surface morphology evolution does not correlate to the corrosion of Si

Firstly, pure hydrofluoric acid can only etch the SiO_x oxide on the nanowire surface but hardly with Si. In our sample, a uniform 1~2 nm SiO_x layer presents on the Si nanowire surface, which cannot account for the observed severe surface morphology changes. Additionally, should certain corrosion reaction happen, Si would be expected to present in the SEI or electrolyte. However, barely any Si is found in the SEI or electrolyte after cycling, as evidenced by the elemental mapping data of the SEI (Fig. 2b) and the inductively coupled plasma mass spectrometry data on the residual electrolyte from a similar cell[1]. Moreover, despite the obvious surface morphology changes, the capacity loss after 36 cycles is very low (~5.6%, see Method for the calculation), indicating that the surface morphology changes are not due to materials loss.

Supplementary Table 1. Parameters used in the simulation of morphological evolution

Parameter	Symbol	Normalization	Value
Energy barrier coefficient	Ω	$\Omega/(c_{\max}\mathrm{RT})$	2.6
Gradient energy coefficient of c_{Li}	κ_{Li}	$\kappa_{\mathrm{Li}}/(c_{\max}\mathrm{RT}l_0^2)$	0.0001
Gradient energy coefficient of c_{v}	κ_{v}	$\kappa_{\mathrm{v}}/(c_{\max}\mathrm{RT}l_0^2)$	0.00001
Volumetric change coefficient	β		0.5874
Elastic modulus of pure/unlithiated silicon	$E_{\max}$	$E_{\max}/(c_{\max}\mathrm{RT})$	175
Elastic modulus of lithiated silicon	$E_{\min}$	$E_{\max}/(c_{\max}\mathrm{RT})$	43.75
Yield strength	σ_{Y}	$\sigma_{\mathrm{Y}}/(c_{\max}\mathrm{RT})$	1.64
Mobility of lithium	M_{Li}	$\mathrm{M}_{\mathrm{Li}}(c_{\max}\mathrm{RT}\Delta t)/l_0^2$	10
Mobility of vacancy	M_{v}	$\mathrm{M}_{\mathrm{v}}(c_{\max}\mathrm{RT}\Delta t)/l_0^2$	0.1
Maximum concentration	$c_{\max}$		0.86
Minimum concentration	$c_{\min}$		0.14

Supplementary Reference

1. Jia, H., et al. Nanostructured $ZnFe_2O_4$ as Anode Material for Lithium-Ion Batteries: Ionic Liquid-Assisted Synthesis and Performance Evaluation with Special Emphasis on Comparative Metal Dissolution. *Acta Chim. Slov.* **63,** 470-483 (2016).